A low-fidelity model for the dynamic analysis of full-lattice wind support structures

Vergassola, Marco; Cabboi, Alessandro; van der Male, Pim; Colomés, Oriol

DOI
10.1016/j.marstruc.2023.103506

Publication date
2023

Document Version
Final published version

Published in
Marine Structures

Marine Structures 92 (2023) 103506

Contents lists available at ScienceDirect

Marine Structures

journal homepage: www.elsevier.com/locate/marstruc

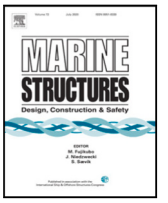

A low-fidelity model for the dynamic analysis of full-lattice wind support structures

Marco Vergassola *, Alessandro Cabboi, Pim van der Male, Oriol Colomés

Faculty of Civil Engineering and Geosciences, Delft University of Technology, Stevinweg 1, 2628CN Delft, Netherlands

ARTICLE INFO

Keywords:
Lattice structures
Wind energy
Model reduction
Structural dynamics

ABSTRACT

This work aims to develop a low-fidelity model for a lattice support structure for offshore wind applications. The proposed low-fidelity model consists of a sequence of regular Timoshenko beams, each of them characterized by homogenized mechanical and mass properties representative of the single bays of the reference space-frame structure. The homogenized elastic coefficients of the sequence of beams are then computed by means of two alternative procedures: case (a), via analytical expressions available in the literature and accounting for a partially isotropic behaviour; case (b) by means of an optimization procedure, with ad hoc calibration factors. The suggested methods to derive the homogenized elastic coefficients are then tested for both straight and tapered lattice structures. The prediction performance is evaluated in terms of estimation of the first five natural frequencies and mode shapes, response to dynamic loads, and ability to predict rotor-structure interaction phenomena. A parametric study is then performed to evaluate the potential and limitations of the proposed models. To bypass the optimization procedure (b), a data-driven approach is also proposed for the case of straight lattice structures.

Overall, the developed low-fidelity model leads to a computational speed-up factor of at least 60. The prediction reliability of the low-fidelity model is discussed for a tapered and regular straight lattice structure. However, for the latter one, a more detailed comparative study between the various modelling assumptions is performed and discussed. With reference to the straight lattice tower, whenever an optimization procedure is used (case (b)), and with reference to a typical subset of the investigated geometrical parameter space, the mean prediction error of the first five natural frequencies is lower than 1%. On the other hand, for case (a) and for the same investigated subset, the mean prediction errors for the first two bending modes and the torsional mode are, 5.2%, 13.3% and 18.8%, respectively. These results are improved in case a data-driven regression model is used to predict the calibration factors, leading to mean prediction errors below 5% for the entire investigated parameter space.

1. Introduction

1.1. General overview of future wind energy scenarios for supporting structures

The turbine sizes within the offshore wind industry are getting larger year by year. In the last decade, between 2010 and 2019, the average size of an offshore wind turbine increased from 3 MW to 6 MW [1]. For the current decade, the market expectation is

* Corresponding author.
E-mail address: M.Vergassola@tudelft.nl (M. Vergassola).

https://doi.org/10.1016/j.marstruc.2023.103506
Received 30 January 2023; Received in revised form 7 July 2023; Accepted 10 August 2023
Available online 1 September 2023

to have a 14 MW wind turbine commercially available by 2024 [2], combined with serial productions of 15 MW turbines [3]. This trend inevitably calls for the development of new modelling strategies able to simulate dynamic responses of support structures, on top of which the wind turbines are installed. The increase in the size of a wind turbine would demand an increase in the size of the supporting monopile, triggering new manufacturing, transportation, installation and design challenges [4,5]. Alternative bottom-fixed solutions to the monopile structures can be sought by deploying support structures such as hybrid jacket-towers [6] or full space-frame structures [7–9]. Among these two solutions, the space-frame structure enables a larger margin for the optimization of its configuration and corresponding mass, generally leading to better design solutions. A further aspect which is of interest for the incoming scenario of wind support structures is related to the use of either a three-bladed or a two-bladed rotor for the wind turbine. The current market seems to favour the three-bladed solution, though, considering the ongoing increase in blade size, the two-bladed rotors are most likely to become more attractive [10,11]. However, whereas two-bladed rotors lower manufacturing and installation costs, control issues related to the dynamic imbalance caused by the time-dependent mass distribution need to be tackled [12].

The above-depicted future scenario suggests that wind turbines and their supporting structure will increase the complexity of their structural behaviour during operational conditions. To account for such complexity, high-fidelity numerical models (HFM) are needed in order to obtain reliable predictions of their mechanical behaviour. However, practitioners often recur to more idealized and low-fidelity models (LFM) developed for specific predictive targets, in order to tackle tasks in which time is the biggest constraint, such as the preliminary design during the tender phase, real-time model updating by means of an incoming data stream from a monitoring campaign [13–15] or sensitivity studies of the parameter space for nonlinear conditions, optimization and uncertainty quantification. For the last three tasks, it is important to highlight that LFMs are also relevant in the context of a multi-fidelity framework in combination with other higher- or lower-fidelity models. Multi-fidelity approaches use LFMs to explore the parametric space, with a few HFMs evaluations to achieve a certain level of accuracy [16]. Such an approach is highly used in wind turbine design optimization, see for instance [17], or uncertainty quantification, see [18].

LFMs should be able to both assess and account for the main static and dynamic behaviour, and for their corresponding sensitivity of the most representative geometrical and mechanical parameters of the structure. For the sake of clarity, throughout the paper, the wording “high” and “low” fidelity model is used to describe, respectively, complex models that require a high computational effort able to simulate a large spectrum of possible nonlinear structural responses, and simplified models validated for a selected range of input and output conditions.

1.2. Low-fidelity modelling for space-frame structures

Low-fidelity models for space-frame structures (e.g. transmission towers, guyed masts) often rely on “user-friendly” analytical expressions, either derived mathematically from structural mechanics principles [19] or empirically by means of regression methods applied to large data sets [20], by identifying existing correlations between the most representative structural parameters and the target dynamic feature, i.e., natural frequency. For both types of models, tuned corrective factors are often used to tailor the predictions to a specific configuration of the structure [19]. However, their prediction power is limited to the first natural frequency.

The development of similar LFMs for offshore wind turbine support structures designed by employing a space-frame concept is less straightforward. In this study, the focus will be on developing an LFM of an assumed challenging case study represented by a space-frame support structure combined with a two-bladed wind turbine (for more details of the assumed case study see [9]). The factors hindering a straightforward development of an LFM for the case study at hand include the time-dependent dynamic properties of the structure (caused by the asymmetries induced by the varying orientation of the rotor-nacelle assembly (RNA), the effects on the dynamic behaviour due to the presence of a taper ratio, the diagonal welded bracings, the non-uniform mass and stiffness distribution and the large aspect-ratio for the main structural elements.

With reference to the literature on aerospace structures, several examples can be found of methods able to develop LFMs of a space-frame structure. Such methods rely on homogenization techniques that allow linking systems with complex geometry to LFMs with a more regular geometry by using equivalent/homogenized mass and mechanical properties. Homogenized models of this type, for lattice structures, were in fact developed in the late 1970s by Noor [21,22]. Noor derived a procedure that allowed to replace of the original space-frame structure with an equivalent continuum beam model, for which a closed-form (exact) solution exists. The expressions of the elastic coefficients of the beam model are linked to the geometrical and mechanical properties of the structural elements of the lattice structure. Note though, that the assumed lattice structure was formed by a repeating cell, with a triangular [21] and rectangular [22] cross-section, in which the connection between the structural elements forming the repeating cell was assumed to be hinged. The validation study showed in [22] exhibited a good match of the first bending and torsional mode between the homogenized continuum beam model and the effective lattice structure, with a maximum error of 2.5% or 4.5% depending on the bay configuration. Besides model comparisons, also experimental cross-validation was carried out by means of dynamic tests of a scaled lattice structure [23], for which the first two modes were fairly matched by an equivalent continuous beam model. The formulation of an equivalent beam model was extended by including the viscous material damping [24] and the application to the case of a rigidly jointed regular lattice structure [25]. For the latter, McCallen [25] showed that to accurately match the dynamic behaviour of a regular rigidly jointed lattice structure, the Timoshenko beam model needs to be enhanced by introducing an additional strain energy term accounting for the shear deformation of a repeating rigidly jointed cell. Homogenization procedures were also sought to offer a quick and reliable way to carry out buckling analysis of the lattice structure [26,27]. In all the previous studies, the equivalence between the lattice structure and the equivalent continuum model was ensured by equating the kinetic and strain energies of the two structures, within a finite element framework. To complement this approach,

alternative homogenization procedures based on spectral elements [28] and transfer matrices [29] were also studied. Note that all the aforementioned homogenization procedures imply that the lattice structure is formed by the regular repetition of a unit cell, and the equivalence between the continuum beam model and the regular lattice structure is ensured as long as there is a high number of repeating cells representing the periodicity of the lattice structure. An illustrative example of the homogenization procedure for offshore space-frame structures was presented in [30], in which a space-frame structure and the corresponding connection with the soil were idealized by adopting an equivalent beam and a set of linear springs. The advantage of the aforementioned techniques in developing a LFM lies in the capacity of the LFM to handle topology changes, e.g. different number of braces, to perform optimization studies and sensitivity analysis. In case of a topology change of the structure, alternative model reduction techniques, such as modal expansion and truncation approach [31], would require the re-definition of the reduced basis and the subsequently solution of an eigenvalue problem. The goal of the proposed low-fidelity model in [30] was to accurately predict the first mode of the structure, taking into account the soil–structure interaction as well. However, more challenging case studies characterized by a higher dynamic complexity would require LFMs able to predict not only the first mode but also the torsional and the second bending mode [9,12] for tapered lattice structures with welded connections.

1.3. Research objectives

Within the depicted framework, this study presents a low-fidelity model of a space-frame structure – either straight or tapered – assembled by means of welded connections, on top of which a rotor can be installed. In particular, the LFM is tested for the case of a two-bladed rotor which introduces additional asymmetries. The LFM is developed to accommodate the need to reliably predict the main dynamic characteristics of interest, with reference to modal analysis, steady-state and turbulent-driven responses for a preliminary design stage. The proposed model also enables the prediction of time-variant modal properties due to time-dependent system parameters resulting from the rotor asymmetries. Such asymmetry is a characteristic of two-bladed turbines that generate a varying yawing and nodding moment of inertia that depend on the rotor's azimuth (or roll) angle [9,12]. In terms of modal analysis, the predictive targets include the first and second-order bending modes and the first torsional mode. The LFM is developed through a sequence of continuous regular beams, each of them governed by homogenized mechanical and mass properties representative of the single bays of the reference space-frame structure. Each homogenized beam of the LFM is simulated by means of a Timoshenko beam element [32]. The elastic coefficients of the equivalent Timoshenko beam, represented by the shear and bending stiffness, are either identified by available analytical expression present in the literature [21,22] and developed for aerospace applications or finely tuned by means of a proposed optimization procedure, leading to ad hoc calibration factors. A parametric study is then carried out to explore a typical parameter input space used during a preliminary design phase. The first aim of this analysis is to assess the applicability of the analytical expressions derived by Noor [21,22] for lattice structure configurations that differ from the ones originally assumed in [21,22]. The elastic coefficients of the equivalent Timoshenko beam predicted by Noor's expression are eventually corrected by optimized calibration factors. The second aim is to identify the optimal subset of the input space for which the proposed corrected expressions [21,22], applied to the developed low-fidelity model, could be used. With reference to the use of ad-hoc calibration factors, the current study proposes a response surface model [33] able to predict ahead the needed calibration factors as a function of the main geometrical properties of the desired space-frame structure. The surface response model is developed by exploiting a training data set generated by simulating the first 5 eigenfrequencies of more than 2000 different types of space-frame structures. Validation of the low-fidelity model is also performed, by comparing its predicted dynamic responses due to periodic and turbulent dynamic loads, versus a complete finite element (FE) model of the assumed case study, and the reliability and accuracy of the predictions are discussed.

2. Description of the low-fidelity model

As already mentioned in Section 1, the developed low-fidelity model is meant to represent the main dynamic properties of a space-frame structure – either straight or tapered – assembled by means of welded connections, on top of which a rotor can be installed. The underlying strategy of developing the low-fidelity model first relies on applying analytical expressions available in the literature (see [21,22]) to first guess the elastic coefficients of the homogenized Timoshenko beam elements. Subsequently, such coefficients are corrected by means of calibration factors obtained after solving an optimization problem. Broadly speaking, optimal values of the unknown elastic parameters of the homogenized Timoshenko beam elements composing the low-fidelity model need to be found, in order to faithfully reproduce the main dynamic properties of the structure at hand. The general framework of the optimization scheme starts by considering the equation of motion of the undamped full-height lattice support structure, i.e. the high-fidelity model, which reads as follows

$$\mathbf{M}\ddot{\mathbf{x}}(t) + \mathbf{K}\mathbf{x}(t) = \mathbf{f}(t), \tag{1}$$

where the time-dependent vector of size n $\mathbf{x}(t)$ contains the degrees of freedom of the system, and an over-dot indicates a derivative with respect to time. The $n \times n$ matrices $\mathbf{M}$ and $\mathbf{K}$ represent the mass and stiffness matrices of the system, respectively. The external load acting on the system is given by the vector of size n $\mathbf{f}(t)$.

The general eigenvalue problem of this full model is given by

$$\left(\mathbf{K} - \lambda_i \mathbf{M}\right) \boldsymbol{\phi}_i = \mathbf{0}, \tag{2}$$

from which the eigenvalues λ_i and eigenvectors $\boldsymbol{\phi}_n$, for $i = 1, 2, \ldots, n$, can be obtained. A similar matrix formulation is adopted for the low-fidelity model that consists of m degrees of freedom, where $m \ll n$. The $m \times m$ mass and stiffness matrices of this reduced system are represented by $\mathbf{M}^*$ and $\mathbf{K}^*$. These are populated according to the finite element representation of a Timoshenko beam element. The single stiffness matrix $\mathbf{k}^*$ for a Timoshenko beam element accounting for six degrees of freedom at each node is

$$\mathbf{k}^* = \begin{bmatrix}
\frac{\gamma_1 EA_{eq}}{l} & & & & & & & & & & & \\
0 & \frac{12\gamma_1 EJ_{eq,z}}{l^3(1+\Phi_{eq,y})} & & & & & & & & & & \\
0 & 0 & \frac{12\gamma_1 EJ_{eq,y}}{l^3(1+\Phi_{eq,z})} & & & & & & & & & \\
0 & 0 & 0 & \frac{\gamma_2 G_z J_{eq,x}}{l} & & & & & & & & \\
0 & 0 & \frac{-6\gamma_1 EJ_{eq,y}}{l^2(1+\Phi_{eq,z})} & 0 & \frac{(4+\Phi_{eq,z})\gamma_1 EJ_{eq,y}}{l(1+\Phi_{eq,z})} & & & & & & & \\
0 & \frac{6\gamma_1 EJ_{eq,z}}{l^2(1+\Phi_{eq,y})} & 0 & 0 & 0 & \frac{(4+\Phi_{eq,y})\gamma_1 EJ_{eq,z}}{l(1+\Phi_{eq,y})} & & & & & & \\
\frac{-\gamma_1 EA_{eq}}{l} & 0 & 0 & 0 & 0 & 0 & \frac{\gamma_1 EA}{l} & & & & & \\
0 & \frac{-12\gamma_1 EJ_{eq,z}}{l^3(1+\Phi_{eq,y})} & 0 & 0 & 0 & \frac{-6\gamma_1 EJ_z}{l^2(1+\Phi_{eq,y})} & 0 & \frac{12\gamma_1 EJ_{eq,z}}{l^3(1+\Phi_{eq,y})} & & & & \\
0 & 0 & \frac{-12\gamma_1 EJ_{eq,y}}{l^3(1+\Phi_{eq,z})} & 0 & \frac{6\gamma_1 EJ_{eq,y}}{l^2(1+\Phi_{eq,z})} & 0 & 0 & 0 & \frac{12\gamma_1 EJ_{eq,y}}{l^3(1+\Phi_{eq,z})} & & & \\
0 & 0 & 0 & \frac{-\gamma_2 G_z J_{eq,x}}{l} & 0 & 0 & 0 & 0 & 0 & \frac{\gamma_2 G_z J_{eq,x}}{l} & & \\
0 & 0 & \frac{-6\gamma_1 EJ_{eq,y}}{l^2(1+\Phi_{eq,z})} & 0 & \frac{(2-\Phi_{eq,z})\gamma_1 EJ_{eq,y}}{l(1+\Phi_{eq,z})} & 0 & 0 & 0 & \frac{6\gamma_1 EJ_{eq,y}}{l^2(1+\Phi_{eq,z})} & 0 & \frac{(4+\Phi_{eq,z})\gamma_1 EJ_{eq,y}}{l(1+\Phi_{eq,z})} & \\
0 & \frac{6\gamma_1 EJ_{eq,z}}{l^2(1+\Phi_{eq,y})} & 0 & 0 & 0 & \frac{(2-\Phi_{eq,y})\gamma_1 EJ_{eq,z}}{l(1+\Phi_{eq,y})} & 0 & \frac{-6\gamma_1 EJ_{eq,z}}{l^2(1+\Phi_{eq,y})} & 0 & 0 & 0 & \frac{(4+\Phi_{eq,y})\gamma_1 EJ_{eq,z}}{l(1+\Phi_{eq,y})}
\end{bmatrix} \tag{3}$$

The $\Phi_{eq,i}$ terms in Eq. (3) stand for $(12\gamma_1 EJ_{\mathrm{eq},i})/(\gamma_3 G_i A_s l^2)$, where i can be in either direction of the beam cross-section plane, i.e., y or z. The parameters, γ_1, γ_2 and γ_3 are the tuning factors and their number depends on the level of anisotropy of the system. The terms E and G are the Young's and shear moduli, J is the second area moment of inertia, l is the length of the element, and A_s is the effective cross-sectional area in shear, defined as $A_s = \kappa_s A$. For a circular cross-section, A, the shear factor κ_s equals 3/4. The mass matrix $\mathbf{M}^*$ is constructed accordingly; however, it does not contain any correction factor. The resulting eigenvalue problem of the condensed version of Eq. (1) is defined by

$$\left(\mathbf{K}(\boldsymbol{\gamma})^* - \lambda_j^* \mathbf{M}^*\right) \boldsymbol{\phi_j}^* = \mathbf{0}, \tag{4}$$

with the eigenvalues λ_j^* and eigenvectors $\boldsymbol{\phi}_j^*$, for $j = 1, 2, \ldots, m$. Here $\boldsymbol{\gamma}$ contains the tuning parameters γ_1, γ_2 and γ_3.

To ensure an equivalence for a given set of predefined modal properties between Eqs. (2) and (4), the elements in matrices $\mathbf{M}^*$ and $\mathbf{K}^*$ should be chosen, such that the eigenvalues λ_j^* and the eigenvectors $\boldsymbol{\phi}_j^*$ equal the predefined set of eigenvalues λ_i and eigenvectors $\boldsymbol{\phi}_i$ of the original system, for $i = 1, 2, \ldots, p$, where $p < m$. Such equivalence is sought by means of minimizing the following objective function ϵ_1

$$\min\ \epsilon_1[\boldsymbol{\gamma}] = \min \sum_{j=1}^{p} \left(1 - \frac{\lambda(\boldsymbol{\gamma})_j^*}{\lambda_j}\right)^2 \tag{5}$$

Eq. (5) minimizes the squared difference between the eigenvalues, enforcing a global match between the two models. However, the minimization process could be constraint more by adding a further cost function involving the eigenvectors, which reads as follows

$$\min\ \epsilon_2[\gamma] = \min\left(\mathbf{I} - \mathrm{MAC}(\boldsymbol{\gamma})\right)^2 \tag{6}$$

where $\mathbf{I}$ is an identity matrix and MAC is the Modal Assurance Criterion matrix [34] defined as

$$\mathrm{MAC} = \frac{|(\boldsymbol{\phi}^*)^H \hat{\boldsymbol{\phi}}|^2}{[(\boldsymbol{\phi}^*)^H \boldsymbol{\phi}^*][\hat{\boldsymbol{\phi}}^H \hat{\boldsymbol{\phi}}]} \tag{7}$$

where the superscript H stands for the Hermitian transpose. In order to compute ϵ_2, it should be noted that the eigenvectors of the HFM used in Eq. (6), denoted as $\hat{\boldsymbol{\phi}}$, are represented by the normalized modal amplitudes of the central longitudinal axis of the structure and the number of modes is p. The use of Eq. (6) either allows for a local improvement of the minimization results or it can serve as a comparative metric to evaluate and locally validate the accuracy of the reduced model.

Generally speaking, structures can exhibit an isotropic, partially isotropic or anisotropic behaviour in shear. If $G_{zx} = G_{yx}$, i.e. the structure is transversely isotropic (partial isotropy), like the discussed case, the minimization process only demands three tuning parameters: γ_1, γ_2 and γ_3. If the structure is isotropic, then a single shear modulus G is required, and γ_2 may equal γ_3. In the case of anisotropic behaviour, then a fourth tuning parameter is necessary. The parameter γ_1 corrects the Young modulus that influences the bending and axial stiffness, parameter γ_2 corrects the shear modulus related to the torsional stiffness, while γ_3 is a corrective factor for the shear modulus responsible for the shear stiffness due to bending. All three tuning parameters are needed in order to correct the equivalent elastic coefficients such as $EJ_{eq,i}$, $GJ_{eq,x}$ and $G_i A_s$. An initial guess of such coefficients can be made by imposing equivalences between the geometrical and inertial properties of the lattice structure's and equivalent beam's cross-section. To start, note that the low-fidelity system is modelled as $\frac{m}{6} - 1$ beam elements since six degrees of freedom are assigned at each node. This implies that m should be chosen sufficiently large so that the desired p eigenvalues and eigenvectors can be approximated sufficiently well. A good approximation is to represent each repetitive block of the structure, called bay, with a beam element like

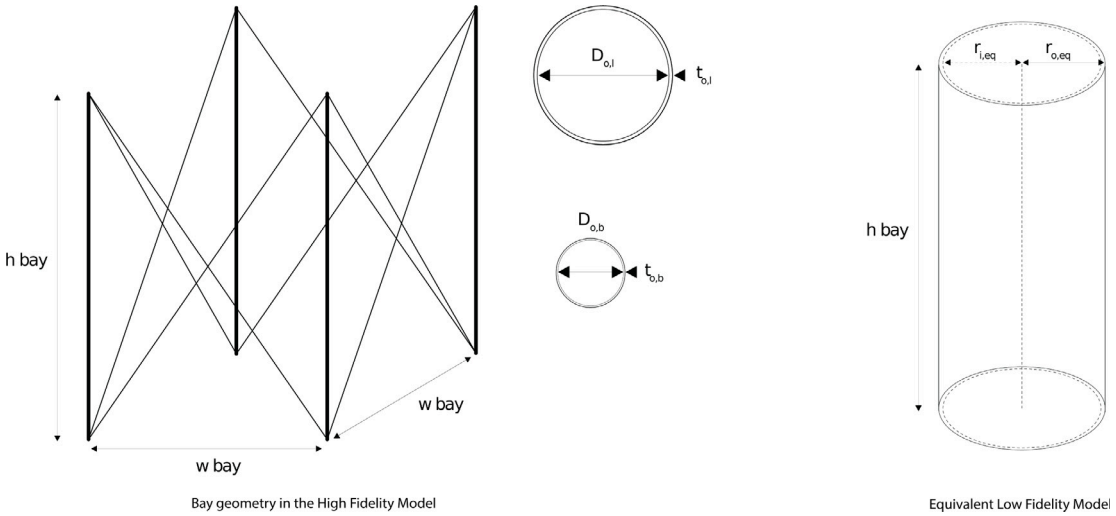

Fig. 1. Example of a bay (left figure) and its equivalent beam (right figure), including a typical cross-section of the main "leg" (with diameter $D_{o,l}$) and brace element with diameter $D_{o,b}$. The equivalent beam is assumed to be a thin-walled cylinder.

shown in Fig. 1. The choice of a cylindrical beam rather than an arbitrary shape lies in the easiness of implementing such elements in most software used for the dynamic analysis of structures. Hence the length l in Eq. (3) corresponds to the length of the main legs and therefore the length of the equivalent beam element. The geometrical details of the cross-section of the equivalent beam element are obtained by means of solving a system of two equivalences, which reads as

$$\begin{cases} \mathbf{J}_{bay,r} - \mathbf{J}_{eq,r} \approx 0 \\ M_{bay,r} - M_{eq,r} \approx 0 \end{cases} \tag{8}$$

where $\mathbf{J}_{i,r}$ and $M_{i,r}$ are the moment of inertia vector and the mass, respectively, computed for either the bay or the equivalent beam. The terms $\mathbf{J}_{eq,r}$ and $M_{eq,r}$ are functions of the unknowns parameters $D_{in,eq}$ and $D_{ou,eq}$, that are the inner and outer diameter, respectively, of the hollow cylindrical beam element. The index r for $\mathbf{J}_{eq,r}$ and $M_{eq,r}$ ranges between $1, \ldots, \frac{m}{6} - 1$, while the moment of inertia vector $\mathbf{J}$ includes $\mathbf{J} = (J_x, J_y, J_z)$. The solution to the minimization problem shown in Eq. (8) provides the geometrical information required to construct the beam element. It should be noted that the minimization problem has four solutions, but only one is in the first quadrant, i.e., it is physically meaningful. This ensures the uniqueness of Eq. (8). For the case in hand, we assumed a welded lattice structure as reference, and two assumptions were introduced to justify the minimization process shown in Eq. (8): (a) the distributed mass of a single beam element is assumed equal to the average distributed mass over the height of the corresponding bay, and (b) the equivalent moments of inertia with respect to x, y and z of the beam element should be equated to the average between the corresponding moments of inertia computed for the bottom and top cross-section at each single bay. For the latter computation, only the main structural legs of the corresponding bay are considered, while the moment of inertia of the braces is neglected. By introducing these assumptions and assuming equal material properties for the two models, we can estimate $D_{in,eq}$ and $D_{out,eq}$, $M_{eq,r}$, l, $\mathbf{J}_{eq,r}$, A_s and A_{eq} for each beam element that is representative of the mass and mechanical properties of a single bay. The set of tuning parameters intends to correct such estimates and improve the model. To facilitate and speed up the minimization of Eq. (5), the equivalent terms that define the shear, $G_i A_s$, and torsional rigidity, $GJ_{eq,x}$, can be first guessed by means of some analytical expressions derived in previous studies [22,25]. As shown in [22], for a regular bay, the terms proportional to the shear and torsional rigidity for an equivalent beam can be analytically computed as

$$G_{\mathrm{i}} A_{\mathrm{s}} = \frac{4 E A_{\mathrm{eq}} h_{\mathrm{bay}} w_{\mathrm{bay}}^2}{l_{\mathrm{b}}^3} \tag{9}$$

and

$$GJ_{\mathrm{eq,x}} = \frac{2 E A_{\mathrm{eq}} h_{\mathrm{bay}} w_{\mathrm{bay}}^4}{l_{\mathrm{b}}^3} \tag{10}$$

where l_b is the length of the brace element. Note that this approximation is only valid for regular pin-jointed lattice structures, with double-laced bays. A more refined expression for $GJ_{eq,x}$, valid for a rigidly jointed lattice tower characterized by bays without braces was provided in [25]. However, for this study, the shear and torsional stiffness terms defined by Eqs. (9) and (10) are used. In Section 4, it will be shown that for very slender structures, the tuning parameters for this initial guess are close to one.

A last remark is devoted to the modelling of the foundations. For the case at hand, the connection between the lattice tower and the soil is assumed to be fixed, hence the same type of boundary condition applies to the equivalent beam model. Note that

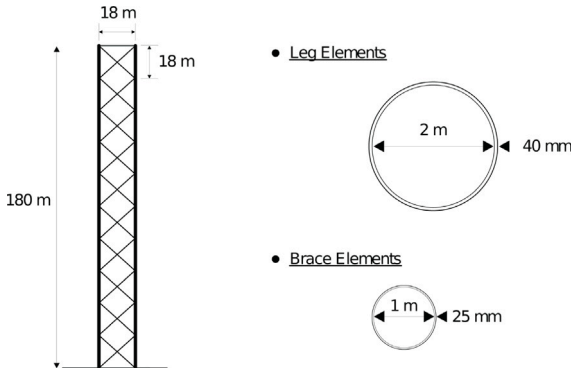

Fig. 2. Geometry of the regular multi-cell 3D frame.

the actual influence of the soil–structure interaction experienced by the lattice tower cannot be translated by applying the same boundary condition to the equivalent beam. The latter equivalence calls for a separate investigation [35].

3. Validation of the low-fidelity models

3.1. Regular multi-cell 3D frame

In this section, a low-fidelity model of a structure is obtained following the steps described in Section 2. The LFM is then validated by comparing its response to a high-fidelity model of the same considered structure. The investigated case study is represented by the lattice tower shown in Fig. 2. This is a regular lattice tower composed of ten equal and squared bays, the exact dimensions are indicated in the corresponding figure. To ensure a thorough validation of the proposed LFM, the complexity of the HFM is gradually increased. Firstly, the structure as presented in Fig. 2 is considered (HFM-RNA0). Then, a point mass is introduced on top of the structure, representative of the translational inertial effect of the RNA (HFM-RNA1). Finally, a more detailed RNA is considered, accounting for the rotational inertial terms as well, i.e., rolling, yaw and, nodding moments of inertia, as well as the eccentricity of the RNA (HFM-RNA2).

A high-fidelity model of HFM-RNA0 can be obtained with any finite element software. Within this study, we used an in-house Matlab-based tool, specifically developed for the dynamic analysis of offshore wind support structures and described in [9]. An LFM of this structure is obtained by minimizing the objective function of Eq. (5) under the assumptions described in Section 2. Here, Eq. (6) is used as a validation metric to evaluate the agreement between the mode shapes of the two models. For the purpose of validation, the comparative analysis between the LFM and HFM encompasses three different aspects: (1) the accuracy of the LFM in capturing the first five eigenfrequencies of the system, (2) the correlation of the corresponding mode shapes between the LFM and HFM, with respect to shape and modal amplitude and, (3) the prediction performance of the LFM in mimicking the dynamic response of the HFM to both periodic and turbulent loads.

With reference to Fig. 2, by solving the system of equations described in Eq. (8), one obtains an equivalent thin-walled cylindrical beam having a radius of 9.3 m and a wall thickness of 31.6 mm. For both models standard steel properties are assumed, i.e. a density of 7850 kg/m^3, Young's modulus of 210 GPa, and Poisson's ratio of 0.3. Shear and torsional rigidity of individual beams composing the HFM-RNA0 are computed as normally for a Timoshenko beam made of isotropic material. For the LFM, $G_{ix}A_s$ and GJ_{eq} are firstly estimated with Eqs. (9) and (10) and then corrected by solving the minimization problem by means of Eq. (5). This last step is only necessary for a specific subset of the design parameter space, as discussed in Section 4. However, since the lattice structure presented in Fig. 2 is connected by welded joints, without the use of horizontal structural elements within bays, it is expected that Eqs. (9) and (10) will not correctly estimate G_iA_s and $GJ_{eq,x}$ for all the modes of interest. Table 1 presents the comparison between the HFM-RNA0 and the corresponding LFM with respect to the first five modes. Modes and corresponding frequencies are computed via modal analysis for both models. The column "first guess" shows the results obtained with the approximation provided by Eqs. (9) and (10). The error is the normalized difference between the estimated natural frequency expressed in percentage. Since the error on both torsional and second bending modes is large, the minimization problem is solved to obtain the tuning parameters γ and improve the corresponding LFM. The minimization is stopped as soon as the error drops below 1% for all the eigenfrequencies. The results of this step are presented in Table 1 under the column "final iteration". The respective tuning factors, γ, are also presented. These results show that for the investigated structure Eqs. (9) and (10) cannot predict properly the frequency of any mode higher than the first pair of bending modes. However, by solving the minimization problem, the shear and torsional rigidity can be corrected to improve the LFM and reach the desired level of accuracy. It should be noted that the focus is only on the first five modes since these are often the most relevant for (offshore) wind turbine systems. Hence, in this study $p = 5$ in Eq. (5).

Table 1
Estimated natural frequencies from HFM-RNA0 and LFM, and corresponding predictive error. For each pair of bending modes, only one frequency is presented since the other one is identical. The natural frequencies are computed via modal analysis.

Frequency	HFM-RNA0 [Hz]	LFM - First guess [Hz]	‖Error‖ [%]	LFM - Final iteration [Hz]	‖Error‖ [%]	γ [–]
1st bending	0.544	0.547	0.65	0.543	0.14	1.01
Torsion	1.919	1.736	9.51	1.919	0.01	1.22
2nd bending	2.708	2.847	5.98	2.712	0.95	0.74

Table 2
Estimated natural frequencies from the HFM and LFM for the case of RNA1 and RNA2, and corresponding predictive error. For the RNA2 case, the frequencies are estimated by assuming a rotor orientation at zero degrees with reference to the azimuth. The natural frequencies are computed via modal analysis.

Frequency	HFM-RNA1 [Hz]	LFM-RNA1 [Hz]	‖Error‖ [%]	HFM-RNA2 [Hz]	LFM-RNA2 [%]	‖Error‖ [–]	γ [–]
1st bending	0.367	0.366	0.15	0.365	0.365	0.08	1.01
	0.367	0.366	0.15	0.367	0.366	0.08	
Torsion	1.919	1.918	0.01	1.177	1.178	0.02	2.10
2nd bending	2.205	2.199	0.22	2.102	2.109	0.33	0.79
	2.205	2.199	0.22	2.196	2.217	0.95	

For the next step, an RNA is placed on top of the structure shown in Fig. 2. Since the structure itself is unchanged, the first guess for the rigidity terms of the LFM is based on the solution of the previous minimization problem (see γ values in Table 1) rather than on Eqs. (9) and (10). An eventual further minimization is performed only if improvements are needed. As mentioned above, the RNA is included in two stages: firstly a simple point mass is added on top of the structure (HFM-RNA1), and then a more detailed representation of the RNA is considered (HFM-RNA2). The RNA of the wind turbine 2B14 is used as reference, this is a 14MW two-bladed wind turbine described in [9]. In both cases, the rigid body representing the RNA is connected to the structure through a rigid and mass-less element. The weight of the RNA is 796 tonnes. Table 2 compares the eigenfrequencies obtained between the HFM and LFM. The left-hand side of the table shows the results for the HFM-RNA1 while the right-hand side presents the comparison for the HFM-RNA2. For the two models referring to RNA1, the presence of a large top mass lowers the natural frequencies of the bending modes but leaves the torsional one unchanged. The effect of the RNA on the two models (HFM and LFM) is almost identical. Therefore, as expected, there is no need to solve a new minimization problem and the same γ coefficients are used, see Table 1 for the tuning factors. Interestingly, if compared to the errors shown in Table 1 for the final iteration, the addition of a large top mass slightly decreases the mismatch between the second-order bending modes of the HFM and LFM models, specifically from an error of 0.95% to 0.22%. This is a direct consequence of the importance that such a large top mass, representing around 25% of the total mass, has on the natural frequencies of the bending modes. In other words, the presence of a large mass due to the RNA masks any small difference between HFM-RNA1 and LFM-RNA1.

For the case of a more detailed RNA, new γ coefficients need to be found. This RNA includes a large yaw moment of inertia which affects largely the torsional mode. Moving from the HFM-RNA1 case to the HFM-RNA2 one, the torsional eigenfrequency drops by 0.7 Hz. However, for the corresponding LFM obtained without updated tuning factors, the eigenfrequency variation is around 1.1 Hz (not shown in Table 2). As a result, iterative runs should be performed to update the γ coefficients. The updated γ values in Table 2 are fairly comparable to the ones shown in Table 1, apart from the tuning factor linked to the torsional mode. For the investigated systems, it is safe to state that the proposed LFM, inclusive of corrective factors, is able to capture the first five eigenfrequencies with high accuracy.

Next, the comparison between the HFM and LFM mode shapes is performed by inspecting eventual differences in terms of the shape along the longitudinal plane and by computing the MAC of the respective mode shape vectors. Fig. 3 presents the normalized mode shapes of the first five modes for the HFM and LFM of two cases represented by RNA0 (graphs on the left side) and RNA2 (graphs on the right side). The mode shapes are normalized by the modal amplitude of the top node of the HFM. For each pair of bending modes, only one is plotted since the other one is orthogonal and identical. The two columns of plots present a very similar situation. Regardless of the presence of the RNA, the bending modes are properly approximated by the LFM. No significant differences in terms of shape can be identified. It can be seen how the presence of the RNA2 seems to improve even further the results. In terms of absolute value of the modal amplitude, no significant differences are found for the bending modes. However, for the torsional case, a clear difference is present. This is due to an underestimation of the modal mass in the LFM for the torsional mode. Three observations lead to this conclusion: (1) the stiffness over mass ratio is correct because the frequency is properly predicted for the torsion; (2) the mass is neither calibrated nor approximated in the LFM; (3) the bending mode shapes are correctly captured and almost one-to-one identical between the two models. Therefore, the difference in the torsional mode shape must be caused by a difference in the modal mass since the stiffness is tuned. This difference is related to the mass distribution in the torsional plane, which is more concentrated towards the centre of torsional rotation for the LFM. Thus, despite having the same frequency, the modal amplitude differs in the two models. It should be noted that the shape itself is instead correct. In fact, if the mode shape obtained with the two models is normalized by its own maximum modal amplitude, then the two mode shapes perfectly match. Despite this difference in the torsional mode shape, the overall results are satisfying and the mode shapes are sufficiently well predicted by the LFM. The overall quality of this prediction is also confirmed by the MAC matrix computed for the mode shapes of the HFM and the

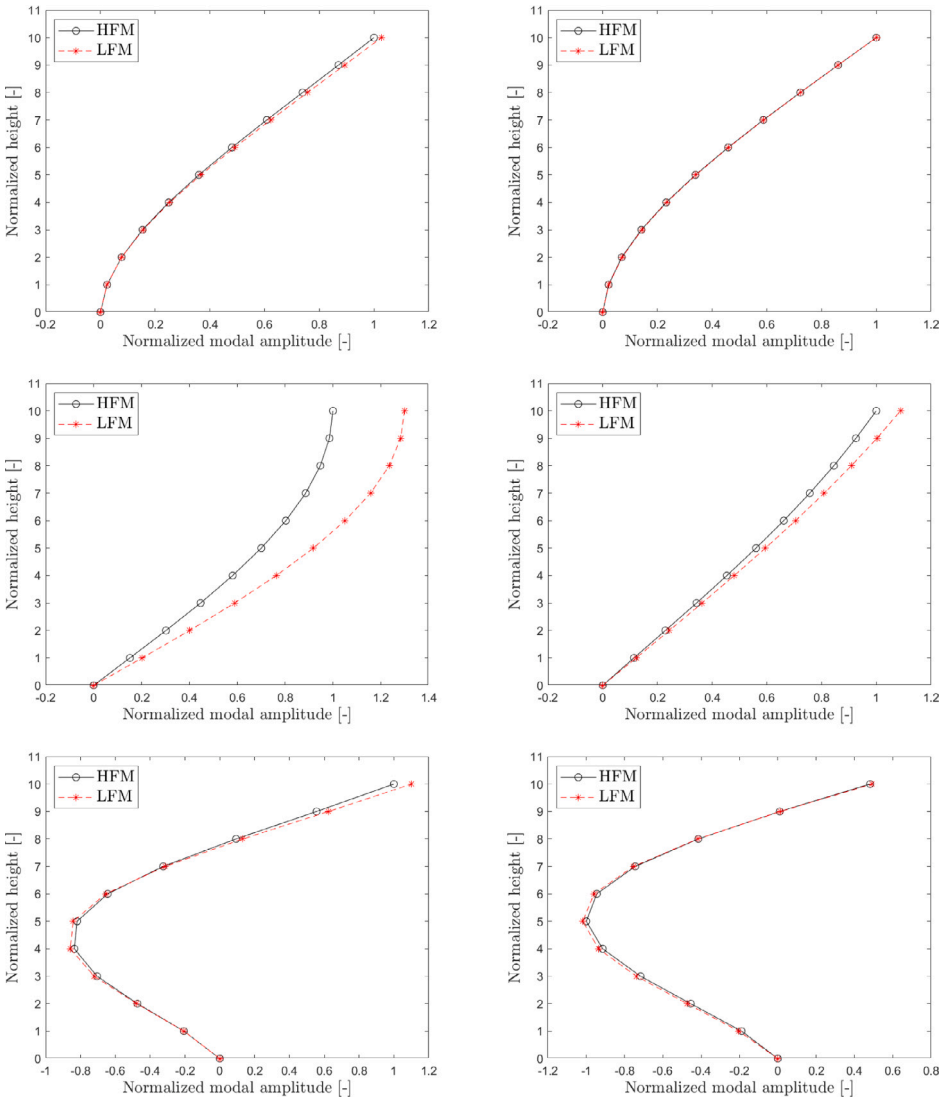

Fig. 3. Two-dimensional normalized mode shapes obtained with the HFM (black) and the LFM (red). First side-side bending (top), torsional mode (middle) and second side-side bending (bottom). The mode shapes relative to the RNA0 and RNA2 cases are presented on the left and right columns, respectively. The mode shapes are normalized by the modal amplitude of the top node of the HFM.

corresponding ones of the LFM. This is presented for the lattice structure alone, $\mathbf{MAC_{RNA0}}$, and for the RNA2 case, $\mathbf{MAC_{RNA2}}$.

$$\mathbf{MAC_{RNA0}} = \begin{bmatrix} 1.0 & 0 & 0 & 0.0087 & 0 \\ 0 & 1.0 & 0 & 0 & 0.0087 \\ 0 & 0 & 0.999 & 0 & 0 \\ 0.0094 & 0 & 0 & 0.999 & 0 \\ 0 & 0.0094 & 0 & 0 & 0.999 \end{bmatrix} \qquad \mathbf{MAC_{RNA2}} = \begin{bmatrix} 1.0 & 0 & 0 & 0.2006 & 0 \\ 0 & 1.0 & 0 & 0 & 0.1721 \\ 0 & 0 & 0.999 & 0 & 0 \\ 0.2104 & 0 & 0 & 0.999 & 0 \\ 0 & 0.1794 & 0 & 0 & 0.999 \end{bmatrix} \tag{11}$$

In both cases, the terms on the diagonal are very close to unity meaning that the mode shapes of the HFM and LFM are consistent. The off-diagonal non-zero terms simply show the partial and negligible resemblance of the first and second bending modes. The proposed LFM was proven to properly capture the global dynamics of the HFM.

Finally, the response of the HFM and LFM to periodic and turbulent loads is investigated. Here, the wording turbulent loads refers to aerodynamic loads considering turbulent flow. For this analysis, the RNA2 case structure is used. This scenario is the closest to a preliminary design phase support structure for wind turbine applications. Regardless of the type of load, this is introduced as a concentrated force applied on the top node of the structure, i.e. at the centre of mass of the RNA. The periodic load is obtained by linearly superimposing six sinusoidal forces whose frequency is a multiple of the assumed rotational speed of the rotor. For a two blades rotor, one should include the rotational frequency of the rotor plus the even multiples of this, i.e. 1P, 2P, 4P, 6P, etc, where

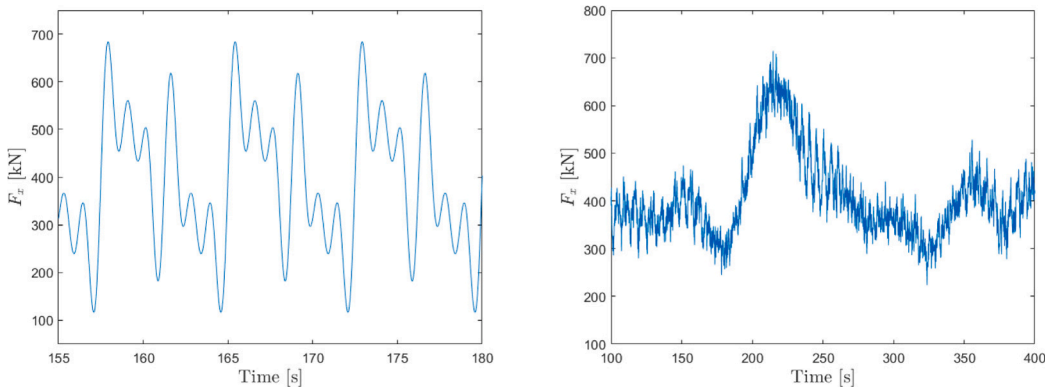

Fig. 4. Example of the periodic (left) and turbulent (right) loads used for the dynamic investigation.

Table 3
Models response to periodic loading and turbulent loading for the presence of a detailed RNA (RNA2) in the model. The displacement values refer to the tower top.

Case	d_{max} [cm]	‖Error‖ [%]	d_{mean} [cm]	‖Error‖ [%]	σ_d [cm]	‖Error‖ [%]	SpeedUp [–]
hfm3	18.9	–	5.24	–	6.05	–	–
lfm3	19.2	−1.4	5.26	−0.4	6.07	−0.4	70
hfm4	20.0	–	5.28	–	7.39	–	–
lfm4	20.3	−1.9	5.29	−0.3	7.37	0.3	71
hfm5	21.4	–	5.26	–	7.94	–	–
lfm5	22.1	−3.5	5.29	−0.4	8.00	−0.7	75
hfm6	23.4	–	5.26	–	8.25	–	–
lfm6	23.3	0.4	5.27	−0.3	8.23	0.2	70
hfm7	15.6	–	5.26	–	4.58	–	–
lfm7	15.8	−1.1	5.28	−0.3	4.59	−0.3	69
hfm8	15.1	–	5.26	–	4.39	–	–
lfm8	15.1	0.2	5.28	−0.4	4.41	−0.4	71
hfmT66	40.9	–	6.49	–	18.5	–	–
lfmT66	44.2	−8.1	6.51	−0.4	19.6	−5.9	72
hfmT6	30.1	–	6.42	–	11.4	–	–
lfmT6	30.6	−1.5	6.44	−0.4	11.6	−1.4	85
hfmT83	78.2	–	16.3	–	28.7	–	–
lfmT83	75.9	2.9	16.4	−0.3	27.6	3.9	66
hfmT8	65.0	–	15.8	–	21.6	–	–
lfmT8	65.8	−1.3	15.9	−0.3	21.8	−0.9	65

P is the rotational frequency. The turbulent loads are obtained from a model of the 2B14 described in [9] via the software Bladed. The structure is considered rigid and fixed at the bottom. A turbulent wind inflow condition is assumed and the resulting loads on top of the structure are extracted. These loads account for the wind turbine dynamics including the aero-servo-elastic effects. Fig. 4 presents an example of the periodic (left) and turbulent (right) loads, respectively. Both systems have zero damping and no further model reduction techniques are implemented. A state-space system is defined for the two structures and their response to the loads is computed numerically with the fourth-order Runge–Kutta method. Table 3 presents the results of the investigated cases in terms of tower top deflections.

The periodic load simulations are run for different rotational speeds of the rotor from 3 to 8 rpm, i.e. covering a common operational regime for large wind turbines. In Table 3, the name of the case indicates the model used, high-fidelity model (hfm) or low-fidelity model (lfm), and the rotor speed. In the case of turbulent loading, a T is added after the model type and the seed number used to generate the turbulent signal is included at the end. If the seed is not indicated, then this means the results presented are averaged over all the seeds. Six seeds are used for each turbulent condition. For instance, for a turbulent load at 8 rpm applied to the high-fidelity model, the resulting case code is hfmT83, if seed 3 is used, and hfmT8 for the averaged results. Seeds are numbers that are used to generate a pseudo-random signal. The use of a seed number to generate the turbulent loads ensures that these results are reproducible. For brevity, in the case of turbulent loading, Table 3 only presents the results related to the seed that leads to the largest displacement and those obtained by averaging the results of all the seeds. Overall, the LFM predicts quite well the displacement obtained with the HFM. For the periodic load cases, both mean value, d_{mean}, and standard deviation, σ_d, of the

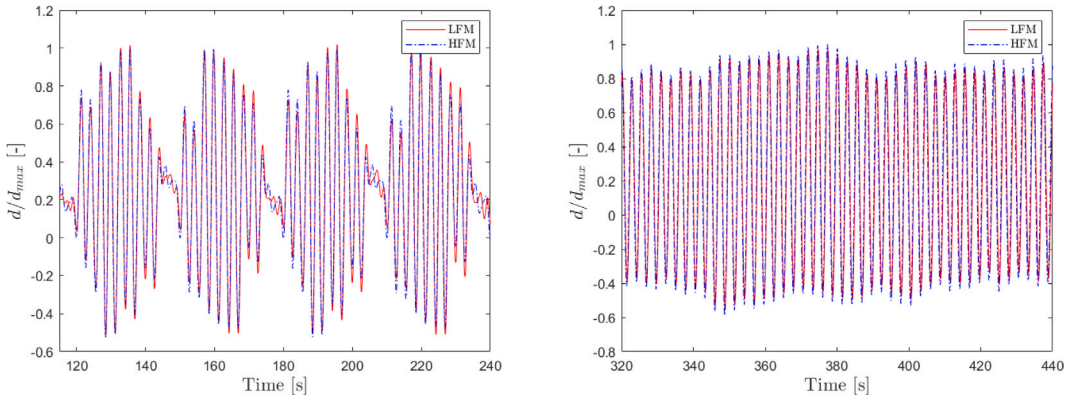

Fig. 5. Time evolution of the normalized fore-aft displacement recorded at the top of the structure for the two models. The figure on the left presents the results of periodic load case h(l)fm5 while the one on the right shows those of the turbulent case h(l)fmt83.

displacements are correctly predicted by the LFM with a maximum error for the standard deviation of 0.7%. For the latter loading case, the maximum displacement estimated by the LFM is in agreement with the HFM but a slightly larger error is observed, i.e. 3.5%. The cases ran with a turbulent load provide a slightly different picture. The mean displacement is still very well predicted by the LFM. However, the accuracy of the LFM concerning the maximum value and the standard deviation of the displacement seems to vary significantly from case to case, with case h(l)fmT66 presenting the largest error, i.e. 8.1%. Nevertheless, when the results are averaged over all the seeds, cases h(l)fmT6 and h(l)fmT8, the two models are in good overall agreement. Finally, considering all the investigated cases, a significant average computational speed up for a factor of 72.8 is achieved with the use of the proposed LFM. Speed-up factors are computed as the ratio between the simulation time of the HFM and that of the LFM. The large speed-up is obtained thanks to the smaller and better-conditioned mass and stiffness matrices of the LFM. In fact, the LFM presents about 51 times fewer matrix entries than the HFM. It should be reminded that this speed-up is obtained without applying any additional model reduction techniques on the two models. Fig. 5 presents the time evolution of the normalized displacement in the horizontal direction recorded at the top of the structure for the cases h(l)fm5, h(l)fmT83. It can be observed, that the LFM mimics quite well the HFM here and the two graphs mostly overlap. For case h(l)fm5, the proximity of the frequency of the third harmonic composing the load, 4P, to the first natural frequency of the system, causes a beating-like phenomenon to appear. For the two latter simulations, Fig. 6 shows the Fourier transform of the displacement. The two figures confirm the quality of the results presented in Table 3. The two models respond to the periodic loads in a very similar manner and all the peaks are identified correctly. From Fig. 6 (left-hand side) the proximity of the load frequency to the natural frequency of the system is easily observed for the case h(l)fm5.

3.2. Tapered multi-cell 3D frame

For the case of a tapered multi-cell structure, the approach presented before remains unchanged. The only difference now is that the geometry of the equivalent beam element varies along the longitudinal axis. The single beam elements used in this study for the LFM are characterized by a constant cross-section, therefore, a representative averaged cross-section for each bay is found. This is achieved by solving Eq. (8) at the top and bottom of each bay and by averaging the result. The same comparative analysis introduced for the regular structure is followed for the tapered one as well. However, in this section, the mode shape correlation in terms of shape and amplitude is not presented to put focus on a few more interesting and complex test cases. In order to assess the accuracy of this methodology for a tapered multi-cell frame, the 2B14 lattice support structure presented in Fig. 7 is used as reference full model. In this subsection, the detailed rotor-nacelle assembly, i.e. RNA2, is used for the entire analysis.

For a detailed description of the design of this structure, the reader is referred to [9]. Firstly, the LFM is constructed and compared against the HFM using the same comparative procedures and metrics presented in Section 3.1. Then the rotor-structure interaction analysis performed in [9] is repeated and extended to further test the limits of the LFM. Table 4 shows the first five eigenfrequencies for both the HFM and the LFM, estimated by assuming a rotor orientation at zero degrees with reference to the azimuth. A rotor azimuth angle of zero degrees corresponds to a horizontal configuration of the blades. The results show that Eqs. (9) and (10), which are derived for a straight bay, fail to predict the torsional rigidity needed to match the torsional model of reference of the tapered structure (see "first guess" column). However, by applying the right tuning factors γ, it is again possible to ensure the desired accuracy for the first five eigenfrequencies (see "final iteration" column). In a previous work [9], it is shown that for a two-bladed rotor rigidly connected to the support structure, the system is time-variant due to the varying inertia caused by the blade rotation. Therefore, it is not possible to define a single set of eigenfrequencies to describe the system. Consequently, if one wants to describe the system with a set of eigenmodes and eigenfrequencies, then this set will depend on the chosen rotor azimuth angle. This dependency is especially pronounced for lattice structures compared to traditional support structures such as monopiles.

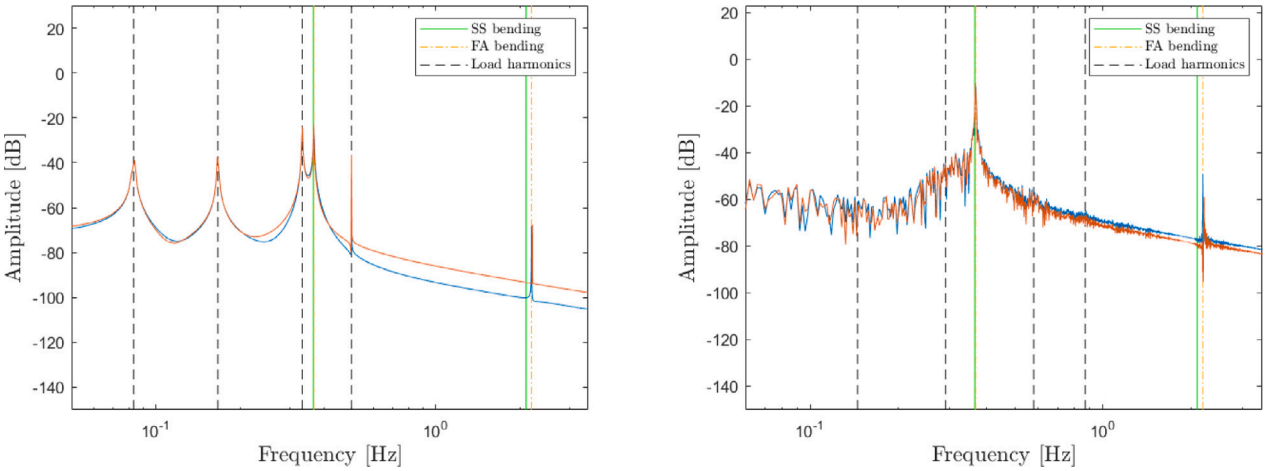

Fig. 6. Fourier transform of the displacement recorded at the top of the structure for the two models. Results of case h(l)fm5 are presented on the left while on the right figure, those of case h(l)fmt83 are shown. The side-side (SS, in green) and fore-aft (FA, in yellow) bending frequencies are obtained from the HFM. The load frequencies are identified by the grey dashed lines.

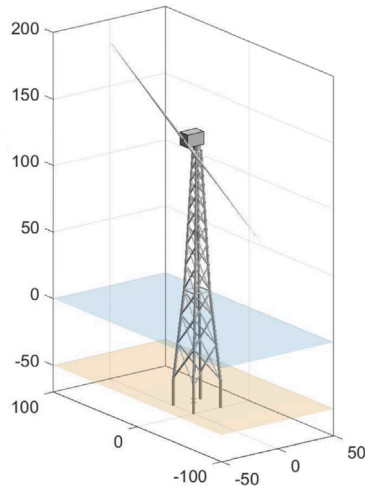

Fig. 7. Full space-frame support structure of the two-bladed offshore wind turbine 2B14 [9].

Since this represents a problem that can affect the design process, it is used as a test case to evaluate the LFM with reference to the HFM predictions. Following the steps described in [9], an eigenvalue analysis as function of the rotor's azimuth position is performed. Figs. 8a and 8b present the variation of the natural frequencies for the low- and high-fidelity model, respectively. It can be seen that apart from small differences in the magnitude, the overall behaviour is well captured by the LFM. The largest discrepancies can be found in the identification of the torsional frequency. This is not surprising since this issue was already discussed in Section 3.1. It should be noted that the error in the torsional modal mass is less significant for the tapered case. Hence the small differences between the two models for varying yaw moment of inertia, i.e. for varying rotor azimuth angle. By inspecting Figs. 8, it can be noticed that all the natural frequencies seem to "cross" each other. As already discussed in [9], the crossing of the natural frequencies is only an apparent behaviour, while the actual underlining phenomenon is linked to the veering of the natural frequencies, due to the lack of symmetry of the structure [36]. Such lack of symmetry induces a slight coupling among the mode shapes, triggering the veering process of the natural frequencies. More specifically, the sequence between the first–second and the fourth–fifth modes are respectively switched between the fore-aft and side-side directions at an azimuth angle next to 60°. The veering is more pronounced for the torsional mode, as shown in Fig. 8. Between an azimuth range of 70–90°, the torsional mode jumps from the third to the fifth position. In addition, at the exact angle of 90°, the torsional mode merges with the side-side second bending mode, emulating a mode coalescence phenomenon [37]. Within this azimuth range, the coupling between the mode shapes of the torsional and second-order bending modes is more pronounced, therefore they cannot be straightforwardly labelled as bending

Table 4
Estimated natural frequencies from the two models. The natural frequencies are computed via modal analysis.

Frequency	HFM [Hz]	LFM - First guess [Hz]	‖Error‖ [%]	LFM - Final iteration [Hz]	‖Error‖ [%]	γ [–]
1st bending SS	0.351	0.339	3.3	0.351	0.05	1.05
1st bending FA	0.355	0.344	3.1	0.355	0.02	
Torsion	0.662	0.473	28	0.662	0.01	2.00
2nd bending SS	1.506	1.433	4.8	1.498	0.51	1.33
2nd bending FA	1.704	1.605	5.8	1.692	0.73	

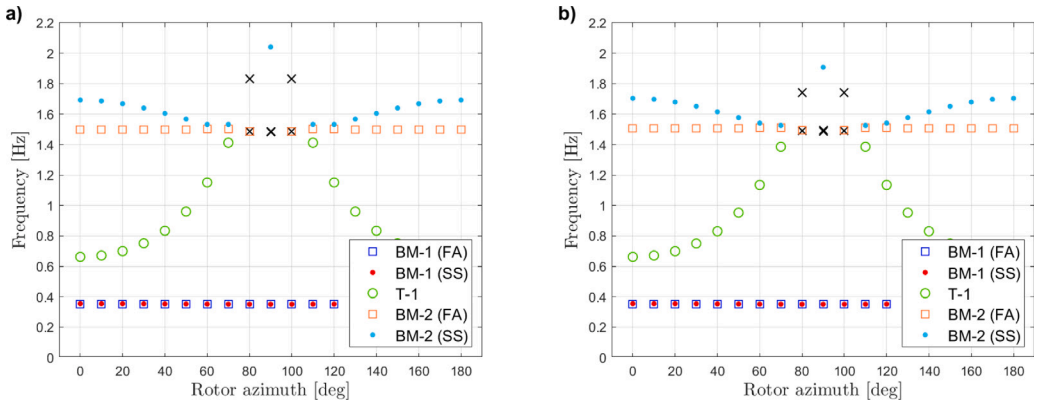

Fig. 8. Variation of the first five mode shape frequencies with reference to an azimuth angle of 0° with (a) corresponding to the LFM and (b) to the HFM. The presented frequencies correspond to the first and second fore-aft (FA) and side-side (SS) bending modes and to the first torsional (T) mode. The black crosses identify hybrid modes that cannot be labelled as either bending or torsional modes.

Table 5
Models response to harmonic loading. The displacement values refer to the tower top.

Case	d_{max} [cm]	‖Error‖ [%]	d_{mean} [cm]	‖Error‖ [%]	σ_d [cm]	‖Error‖ [%]	SpeedUp [–]
hfm3	18.9	–	5.24	–	6.05	–	–
lfm3	19.2	−1.4	5.26	−0.4	6.07	−0.4	63
hfm5	20.0	–	5.28	–	7.39	–	–
lfm5	20.3	−1.9	5.29	−0.3	7.37	0.3	60
hfm8	21.4	–	5.26	–	7.94	–	–
lfm8	22.1	−3.5	5.29	−0.4	8.00	−0.7	61

or torsion. The black crosses in Fig. 8 highlight the aforementioned coupled modes. For a more detailed analysis with respect to the coupling or hybridization of the mode shapes during the veering process, the reader is referred to a previous study in such regard, see [9].

The LFM is then tested for a dynamic simulation including the effect of the time-dependent RNA properties in the system. The investigated cases and results are presented in Table 5. The case labelling follows the same rules presented in Section 3.1. The same load scenarios are applied here as well. Fig. 9 shows the normalized displacement at the top of the structure in the direction of application of the harmonic load, i.e. fore-aft direction. Fig. 10 presents the spectrum of the response. It can be seen that the two models agree quite well in the considered frequency range. However, for frequencies above 1 Hz, the amplitude of the response can differ significantly between the two models despite the correct identification of the location of the peaks. The benefit of using the LFM lies in its simplicity and its lower computation cost with respect to the HFM. This is reflected in smaller and better-conditioned **M** and **K** for the LFM, which have 53 times fewer entries than those of the HFM, and confirmed by the significant speed-up. In fact, for a simulation length of 80 s, the wall time required to solve the HFM is around 10000 s while the LFM takes only 160 s. Therefore, it is clear that the LFM could be very useful whenever several iterations are required. It goes without saying, that the saving in terms of computational cost comes with a lower accuracy of the model for the analysed conditions. However, the extent to which this is relevant depends on the scope of the performed analysis.

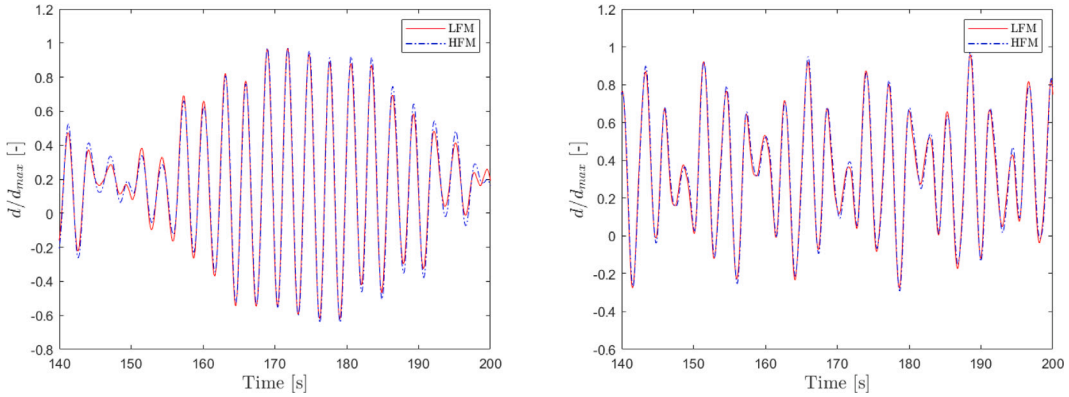

Fig. 9. Time evolution of the normalized fore-aft displacement recorded at the top of the structure for the two models. The left figure presents the results of periodic load case h(l)fm5 while the right one shows those of the turbulent case h(l)fm8.

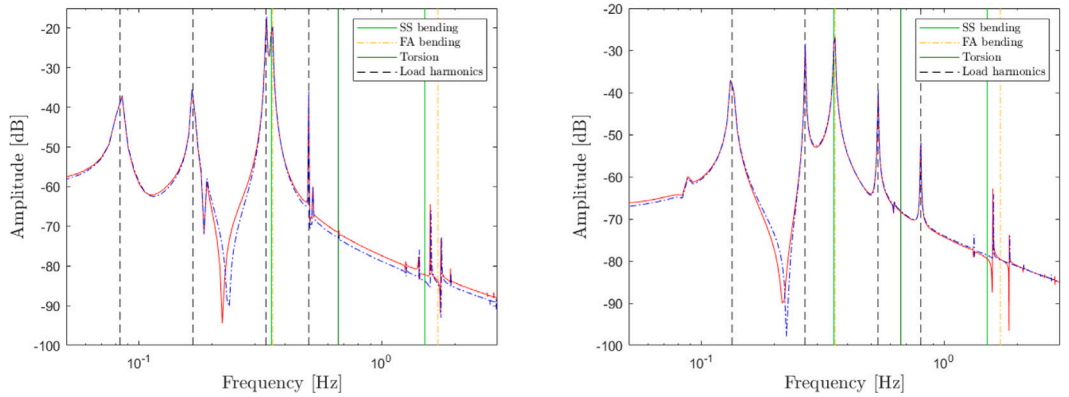

Fig. 10. Fourier transform of the displacement recorded at the top of the structure for the two models. The figure on the left presents the results of case h(l)fm5 while the one on the right shows those of case h(l)fm8. The side-side (SS, in light green) and fore-aft (FA, in yellow) bending frequencies, as well as the torsional frequency (dark green), are obtained from the HFM. The load frequencies are identified by the grey dashed lines.

4. Parametric study

4.1. Potential and limitations of the LFM

In the previous sections, the proposed low-fidelity model was proven and tested under realistic forcing scenarios. In this section, the limitations and potential extensions of this approach are explored. It was shown previously that by adopting an optimal set of calibration factors, γ, it is possible to correct the elastic properties of the equivalent beam (LFM) to match mode shapes and natural frequencies of the HFM when needed. However, the calibration process may represent a limitation in itself for some specific applications. In fact, problems arise whenever information regarding the natural frequencies of interest from the structure of reference is unknown, i.e. whenever an HFM is not available or when the real structure does not exist. Before providing a possible solution to this potential pitfall, this subsection presents a parametric study, in order to assess the parameter space for which it is sufficient to apply Eqs. (9) and (10) to accurately catch the global dynamics of the desired structure. For the latter case, no calibration factors would be needed.

For the following analysis, the presence of the RNA was not taken into account, since the RNA inertial properties would depend on the specific size of each assumed geometrical configuration of the parametric study. The geometric parameters that were considered in this study are: leg and brace diameters, width and height of the bay and total height of the structure. In the case of a regular straight tower, varying the height of the structure is equivalent to changing the number of bays. In addition to these, the batter angle of the structure was added to the list of varying parameters for the case of a tapered tower. The diameter over thickness ratio

was kept constant for both legs and braces because of its little influence on the first few global modes. In this analysis, these were set to 50 and 60, respectively. The braces' diameter could vary between 0.5 and 1.5 m while the legs' diameter varied between 1 and 3.5 m. The total height of the considered structures ranges from 16 to 264 m. A wide variety of bay geometries were considered, all falling between $h_{bay}/w_{bay} = 0.8$ to $h_{bay}/w_{bay} = 2.5$. Both h_{bay} and w_{bay} could run between 4 m and 22 m. Two constraints are then imposed to ensure that unrealistic structures are not considered. Specifically, (1) the D_{legs}/D_{braces} ratio must be larger than or equal to one and (2) the H/w_{bay} should be larger than one.

The contour plots in Fig. 11 show the accuracy of the developed LFM for a large set of virtual regular straight towers. The contour lines represent the error expressed in percentage of the normalized difference between the eigenfrequencies estimated between the HFM and the LFM, as a function of the number of bays, H/h_{bay}, and the local slenderness ratio, here defined as h_{bay}/w_{bay}. On the left column of the contour plots, the elastic properties of the beam are directly obtained from Eq. (8), while on the right one, the elastic properties of the beam element are corrected with Eqs. (9) and (10). Moving from top to bottom, the plots present the error relative to the first (a), third (b) and fourth (c) eigenfrequencies, i.e. first bending, torsion and second bending mode. The contour plots are obtained by assuming the legs and braces diameters equal respectively 2 m and 1 m, while h_{bay} is set to 18 m. Among the various contour plots that can be obtained, the highlighted case in Fig. 11 is selected as representative of the trend observed in most of the sampled geometrical configurations of the regular straight tower.

By inspecting first the contour plots of the left column, it can be observed that the error decrease for increasing number of bays, i.e. for increasing slenderness of the structure. This trend is expected since for increasing slenderness the reference lattice structure behaves more similarly to an equivalent beam. From the right column of Fig. 11, it becomes evident that by correcting the elastic properties of the LFM through Eqs. (9) and (10), the prediction performance significantly improves. Nevertheless, for the first and third modes, the improvements in the prediction performance do not exhibit the same trend observed for the contour plots on the left column, with respect to an increase in slenderness and number of bays. However, it can be concluded that (1) it is possible to identify a parameter space for the first- and second-order bending mode, with a prediction error less than 5%, (2) the error in the estimation of the third mode is always larger than 5%.

As mentioned above, only a representative subspace of the investigated parameter space was shown in Fig. 11. To provide the general trend for all the investigated geometrical configurations, for which Eqs. (9) and (10) were used to correct the elastic properties of the beam, the mean prediction error for the target natural frequencies is found to be 5.2%, 18.8% and 13.3% for the first, third and fourth mode, respectively. Whereas the standard deviation equals 6.5%, 13.3% and 16.8% for the aforementioned modes.

With the aim of confining a more specific parameter space for which the low-fidelity modelling strategy (enhanced by the use of Eqs. (9) and (10)) may be applicable, two subsets of virtual structures were considered. The first subset is defined by imposing the condition that $1 \leq D_{legs}/D_{braces} \leq 2.5$. The second subset is obtained from the first one by adding two extra constraints, i.e. $7 \leq n_{bays} \leq 12$ and $1 \leq h_{bay}/w_{bay} \leq 2$. It should be noted that these constraints are not very limiting in terms of design choices since most (offshore) wind support structures would fall into the second subset. For the different prediction errors of each virtual structure belonging to both subsets, the average relative error $\bar{\epsilon}$, the standard deviation $\sigma_{|\epsilon|}$ and the confidence interval CI were estimated and reported in Table 6. By inspecting the general statistical image of the two subsets, it can be observed that the reliability of the LFM increases while reducing the size of the set. With reference to subset 2, for the first mode, the reliability is relatively high as it is possible to predict this mode with an error below 5% in 83% of the cases of the second subset. However, for the other two modes, the reliability remains low. A similar analysis as depicted in Fig. 11 was carried out for the case of tapered lattice structures. Fig. 12 presents the prediction error on the estimation of the first (a), third (b) and fourth (c) eigenfrequency, respectively. On the left column of contour plots, the elastic properties of the homogenized beam are directly obtained from Eq. (8), while on the right column, the elastic properties of the beam are corrected with Eqs. (9) and (10). Once again, the legs' and braces' diameters are kept constant and equal to 2 m and 1 m for the selected representative case. It should be noted that the bay height is variable for a tapered structure. Specifically, the height of the bay i is computed as $h_{bay,i} = m_h h_{bay,1}$, for $i = 2, \ldots, n_{bay}$, where $m_h = (W_{top}/W_{bottom})^{(1/n_{bay})}$ and $h_{bay,1} = H/\sum_{i=0}^{n_{bay}-1} m_h^i$. Therefore, the bay heights are not directly constrained, but, for a given number of bays, their value depends on the structure height, bottom width and batter angle. In this case, and contrary to what was observed in Fig. 11, the prediction error improves with increasing slenderness of the virtual structure for both types of LFMs. Furthermore, With reference to the right column, the error on the second-order bending mode is quite low in a large area of the plot compared to the straight lattice structure case. However, for the estimation of the eigenfrequency of the torsional mode, the error is once

Table 6
Statistical results of the parametric study for two different subsets for a regular straight lattice structure. The prediction error refers to an enhanced LFM by means of Eq. (9) and Eq. (10).

Relative error ϵ	Subset 1			Subset 2		
	1st bending	Torsion	2nd bending	1st bending	Torsion	2nd bending
$\lvert\bar{\epsilon}\rvert$	3.2	13.9	11.8	2.8	12.7	5.6
$\sigma_{\lvert\epsilon\rvert}$	3.5	7.8	19.0	3.2	7.6	7.1
CI: $\lvert\epsilon\rvert < 5\%$	0.80	0.08	0.44	0.83	0.13	0.64

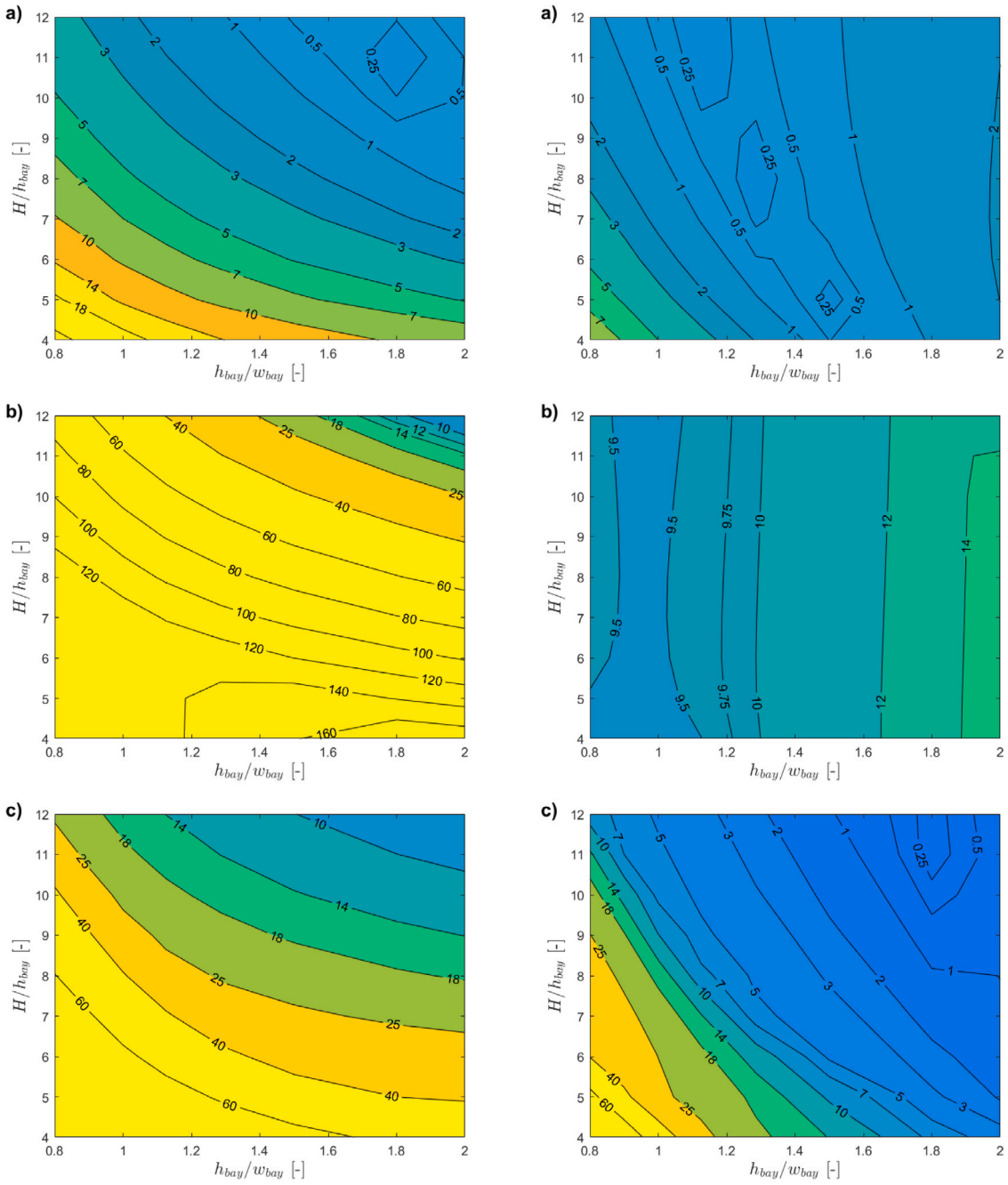

Fig. 11. Contour plots of the error over the estimation of the first (a), third (b) and fourth (c) eigenfrequencies for a regular straight tower. Elements cross-sections and bay height are kept constant. On the left, the beam elastic properties are directly obtained from Eq. (8). On the right, the beam elastic properties are corrected with Eqs. (9) and (10).

again large. To provide a more general statistical image for all the considered cases beyond the depicted one in Fig. 12, and with reference to LFM enhanced by Eqs. (9) and (10), the mean error is found to be 6.0%, 14.7% and 8.7% for the first, third and fourth mode, respectively. Whereas the standard deviation equals 5.6%, 12.2% and 13.5% for the three modes. Although slightly better, these results are in line with those found for the case of straight structures.

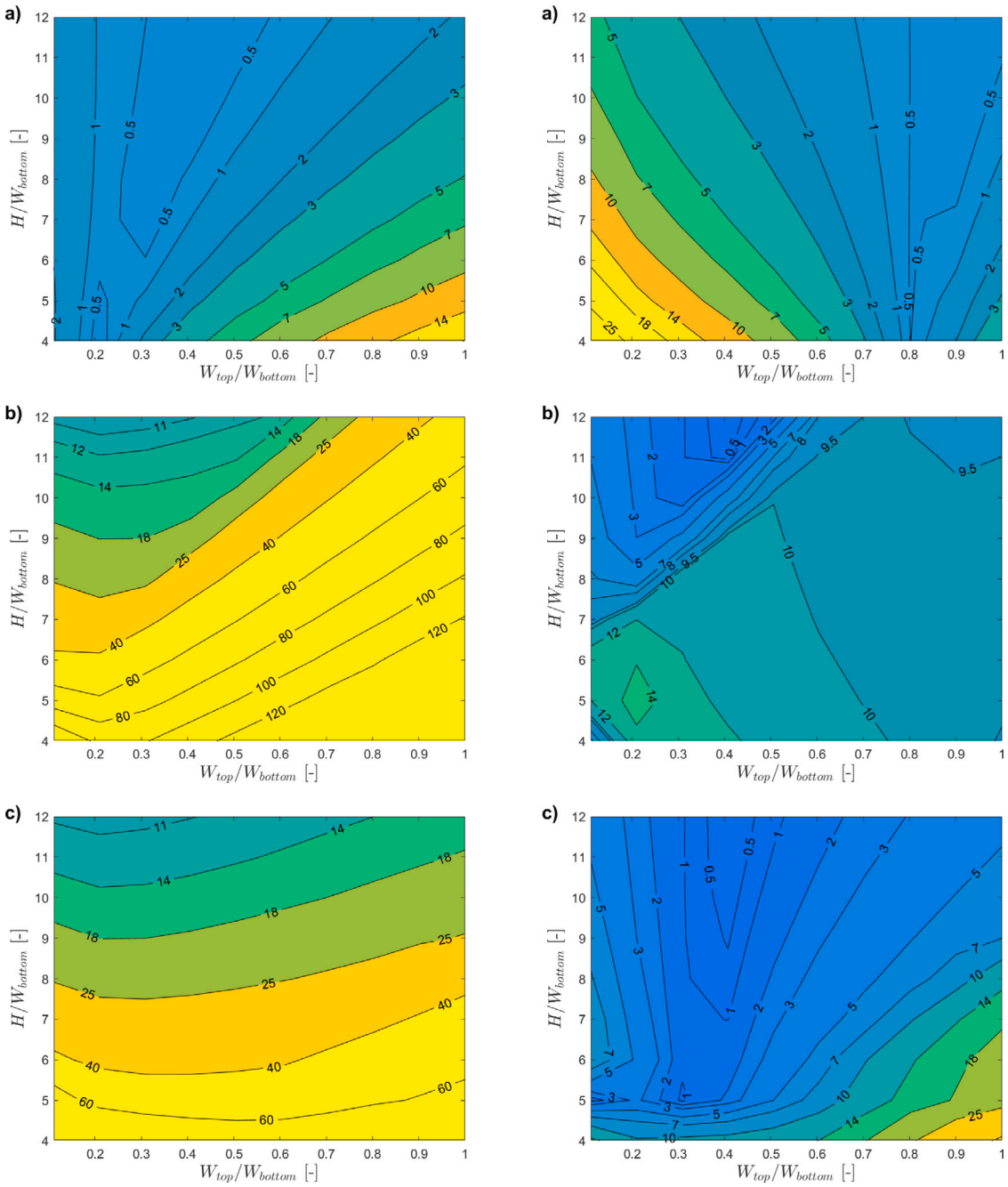

Fig. 12. Contour plots of the error over the estimation of the first (a), third (b) and fourth (c) eigenfrequencies for a tapered lattice tower. The elements cross-sections are kept constant. On the left, the beam properties are directly obtained from Eq. (8). On the right, the beam properties are corrected with Eqs. (9) and (10).

4.2. Response surface modelling for the calibration factors γ

As stated previously, the use of the calibration factors γ enables the identification of the optimal elastic properties of the beam in order to match the eigenfrequencies and modes of the HFM by means of an LFM. However, this may not always be a viable option due to the lack of input needed to carry out the calibration process. This could be the case, for instance, during certain phases of

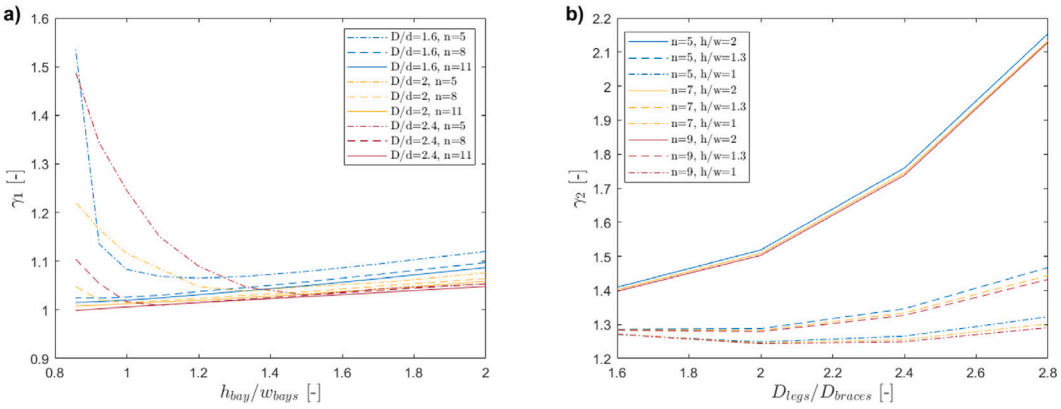

Fig. 13. Figure (a) shows the correlation between the target γ_1 and the predictor w_{bay} for various n_{bay} and D_{legs}/D_{braces} ratios. Figure (b) shows the correlation between the target γ_2 and the predictor D_{legs} for various h_{bay}/w_{bay} ratios and n_{bays}.

a preliminary design. In such a case, it would be ideal to still be able to derive an LFM which is accurate enough. Yet, the above analysis says that the use of Eqs. (9) and (10) alone is not sufficient if the torsional mode is included in the list of target natural frequencies. To enhance the prediction performance, the calibration factors γ would still be needed. Therefore, the aim of this subsection is to propose a response surface model [33] in order to predict the needed calibration factors as a function of the chosen geometrical configuration of the structure to be designed. The development of a response surface model is based on a multivariate regression analysis [33]. It goes without saying that a more detailed analysis could be performed by means of regression analysis based on a Gaussian process [38]. However, such analysis falls outside the scope of the current work, which aim is to first explore whether or not a response surface model could be a convenient tool to determine the calibration factors.

To cope with the large parameter space investigated in Section 4.1 (see subset 1 and subset 2 of Table 6), the multivariate regression is performed with an expression of the polynomial form, and for the sake of simplicity, the analysis is performed for a regular straight lattice tower only. The targets, or dependent variables, of the multivariate regression, are γ_1, γ_2 and γ_3. The set of potential predictors, or independent variables, consists of the legs and braces diameter, height and width of the bay and the height of the structure, i.e. the number of bays. Before performing the multivariate regression, a correlation analysis is carried out. This enables one to identify the relation between predictors and targets and identify potential multicollinearity problems [39]. Fig. 13 presents a predictor-to-target relation that is representative of the general trend observed in the data used for the regression analysis. It should be noted that only a small amount of data are shown here to make the plots less dense and easy to interpret. In Fig. 13(b), the predictor D_{legs} is expressed as a D_{legs}/D_{braces} ratio to make the two figures more easily comparable since the ratio is a parameter in Fig. 13(a) as well (see legend on the top). In the latter ratio, the predictor D_{braces} is kept constant and equal to 1.25 m so that for each line the variable predictor is effectively D_{legs}. Similarly, in Fig. 13(a) h_{bay} is kept constant and equal to 18 m and, for each line, the only variable predictor is w_{bay}. Fig. 13 highlights that for a shorter structure, the relation between γ_1 and w_{bay} is nonlinear, while a linear trend is observed for taller structures. In addition, for higher D_{legs}/D_{braces} ratios and taller structures, the calibration factor γ_1 tends to decrease and approach 1 (see Fig. 13a). A kind of convergence for large values of the h_{bay}/w_{bay} ratio is also observed for the curves at different n_{bays}. Fig. 13(b) shows that the relation between γ_1 and D_{legs} is always nonlinear regardless of n_{bays}. This time, the h_{bay}/w_{bay} ratio is the term affecting this relation the most. It is clear from Fig. 13 that not only the relation between predictors and targets is nonlinear but also that multiple interaction effects are present. An interaction effect occurs when one or more predictors affect how another predictor is related to the target. The presence of these interaction effects means that it will be necessary to include interaction, or coupled, terms in our regression analysis. The nonlinear relations between predictors and targets clearly indicate that at least second-order terms should be considered in the polynomial regression. Higher-order terms could also be used and they might improve the results. However, high-order terms also introduce oscillations in the results and will be therefore avoided. Below, a general representation of the polynomial function to be fitted is shown

$$y_j = p_j(x_1, x_2, x_3, x_4, x_5) + \epsilon, \tag{12}$$

where x_i and y_j define the predictors and the targets, respectively, and ϵ is the fitting error. In an explicit and compact formulation, the polynomial function is expressed as

$$y_{1,2,3} = \sum_{h=0}^{m}\sum_{i=0}^{n}\sum_{j=0}^{p}\sum_{k=0}^{q}\sum_{l=0}^{r}\beta_{h,i,j,k,l}x_1^h x_2^i x_3^j x_4^k x_5^l, \tag{13}$$

where the m, n, p, q and r are the maximum polynomial orders associated to each predictor. In this case, these are all equal to 2. The polynomial expression is truncated such that interaction terms can only describe the interaction between predictor pairs. The least-square method can be used to find the β coefficients (weights) of the three polynomial equations. The coefficients obtained for each target are presented in Appendix, see Table A.8. In this table, the predictors x_1, x_2, x_3, x_4 and x_5 correspond to w_{bay}, h_{bay}, n_{bays},

Table 7
Statistical results of the parametric study for two different subsets for a regular straight lattice structure. The prediction error refers to a calibrated LFM. The calibration factors were obtained by means of Eq. (13).

Relative error ϵ	Subset 1			Subset 2		
	1st bending	Torsion	2nd bending	1st bending	Torsion	2nd bending
$\lvert\bar{\epsilon}\rvert$	1.5	4.1	3.4	0.7	3.0	1.9
$\sigma_{\lvert\epsilon\rvert}$	3.9	5.1	6.0	1.1	3.3	3.3
CI: $\lvert\epsilon\rvert < 5\%$	0.95	0.74	0.82	0.99	0.84	0.91

D_{legs} and D_{braces}, respectively. Thanks to a t-test [39] against a coefficient being zero., it is possible to reduce the number of model coefficients without losing accuracy. This process led to the elimination of one coefficient in each equation, i.e. leaving 20 non-zero coefficients in each equation. Note that further statistical tests can be used to tackle the problem of multiple comparisons, eventually present in the data. However, this falls outside of the scope of this work, since the aim of this subsection is to merely showcase the feasibility of developing a regression model to predict the calibration factors. The obtained polynomial equations were then used to predict the calibration factors γ to improve the prediction errors shown in Fig. 11 and Table 6. Fig. 14 presents a comparison between the right column of Fig. 11 and the contour plots obtained by correcting the beam elastic properties with the predicted γ coefficients. The improvement of the prediction performance is clearly visible for all the considered natural frequencies. Still, larger errors for very short and wide structures are observed, regardless of the use of calibration factors. It is worth underlining that the small parameters space exhibiting larger errors are atypical and therefore not relevant for (offshore) wind support structures. Finally, Table 7 presents an overview of the statistical image of the prediction performance for the two subsets previously introduced. Low error levels were achieved, especially in the second subset, and most of the structures can be properly described by the calibrated LFM. Of course, it is possible that by increasing the number of predictors and polynomial terms one would achieve even better results. However, this would also increase the complexity of the model and reduce its practicality. It is worth mentioning that besides the use of such type of LFM (enhanced by the use of calibration factors obtained through Eq. (13)) during a preliminary design phase, it may also serve as a suitable tool for SHM strategies that may necessitate for real-time processing of acquired monitoring data and online model updating [40]. Note that the data used for the multivariate regression analysis and the script developed to generate the LFMs can be found on 4TU.ResearchData [41] and github [42] respectively.

5. Discussion and conclusions

5.1. Discussion, limitations and future work

The main assumptions, advantages and limitations of the proposed low-fidelity model (LFM) are discussed in this subsection. As discussed in Section 4, to obtain a reliable LFM, either an optimization procedure needs to be applied, if the reference natural frequencies are known, or calibration factors need to be used. Among the main advantages of the developed LFM, it is worth highlighting the capacity to handle topology changes, optimization studies and sensitivity analysis. This advantage emerges provided the developed LFM leads to prediction errors below 5% within a parameter space that well represents the possible geometrical configuration of a wind turbine support structure. On top of that, a large speed-up is obtained due to the smaller and better-conditioned mass and stiffness matrices of the LFM. The large speed-up also favours the use of the LFM in case nonlinearities or more complex damping models are required. In fact, any type of damping can be easily included in the LFM. In the case of Rayleigh damping, this would be implemented in a classical way since such damping is proportional to $\mathbf{M}$ and $\mathbf{K}$. Therefore, one would account for Rayleigh damping in the same manner for the two models. An advantage of this LFM is that local and/or nonlinear damping can also be implemented without the use of any special technique. In fact, thanks to the reduced size of the LFM, the system can be efficiently solved with direct numerical integration methods.

The main evident assumption in the derivation of the low-fidelity model consists of neglecting the moment of inertia of the braces in Eq. (8). While such inertia contribution is straightforward to compute for a straight lattice structure and not too complicated for a tapered one, preliminary calculations suggested not to account for this contribution. In fact, when accounting for the braces contribution, estimating the first natural frequency led to higher errors, around $10+\%$ (without calibration factors). Moreover, also the estimation of the torsional frequency did not improve and only the estimation of the second bending mode frequency improved when accounting for the braces. Of course, one could argue that since a minimization problem is solved to obtain calibration factors, one could account for the braces and let the optimization reduce the discrepancy. However, when solving such a problem, one should wonder if a coupling between the modes exists and whether this can lead to the failure of the optimization process. In the investigated case, the stiffness terms affecting the two bending modes are related to each other; therefore, one cannot tune one frequency without affecting the other one as well. Hence, it is important that the geometric homogenization leads to manageable errors in the first estimation of the frequencies of the two bending modes. Based on preliminary studies, this is the case when the moment of inertia of the braces is neglected. It should also be noted that a relatively large error in the estimation of the torsional frequency does not lead to the same problem since this mode is uncoupled from the bending ones for a beam structure.

Among the modelling choices, only the stiffness matrix was corrected by means of calibration factors. This led to the difference in modal amplitude for the torsional mode discussed Section 3. Such error is due to an underestimation of the modal mass in the LFM for the torsional mode caused by a different mass distribution in the plane of torsional rotation. It should be mentioned that

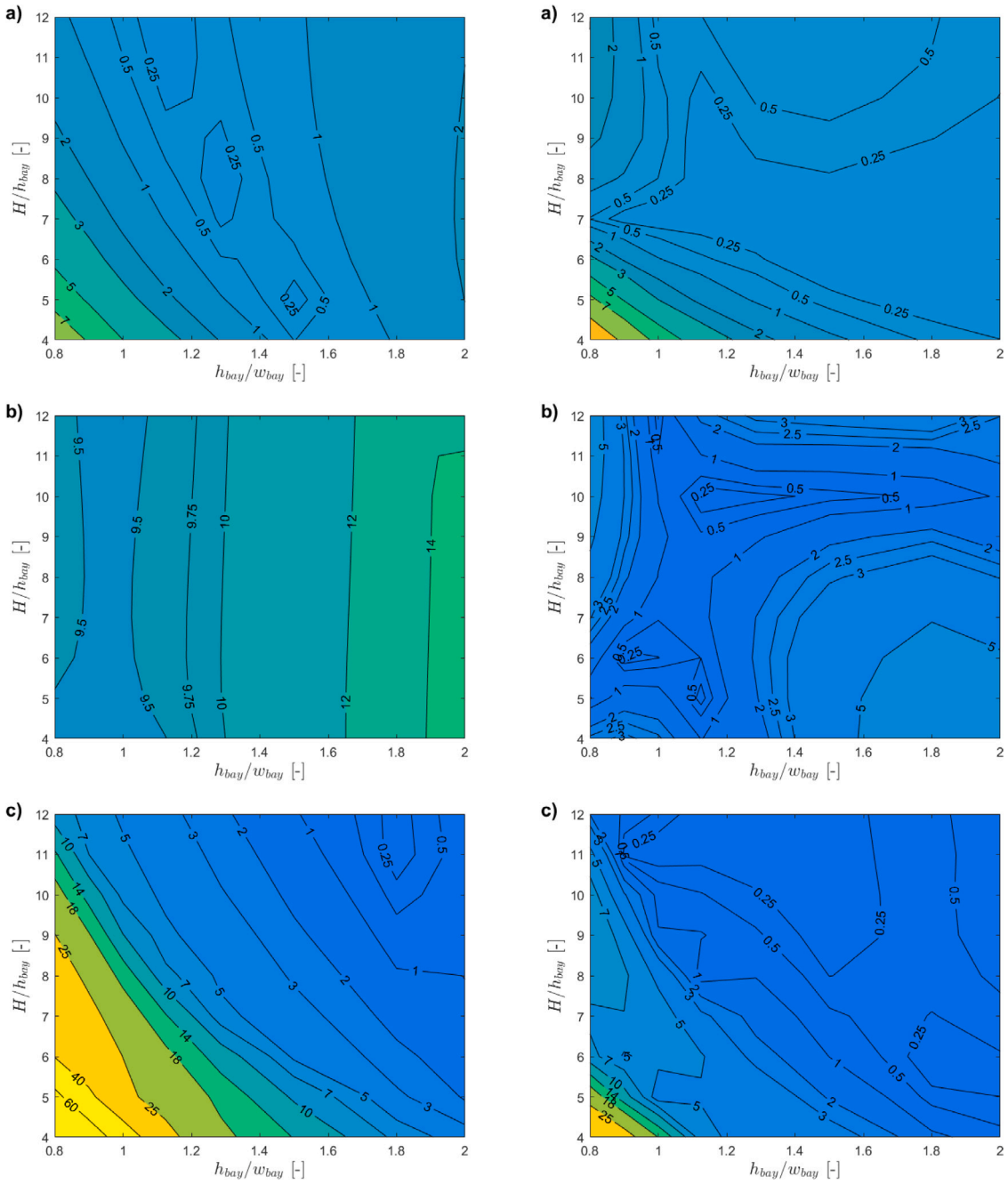

Fig. 14. Contour plots of the error over the estimation of the first (a), third (b) and fourth (c) eigenfrequencies for a regular straight tower. Elements cross-sections and bay height are kept constant. On the left, the elastic properties of the beam are corrected with Eqs. (9) and (10). On the right, these properties are corrected with the γ coefficients computed with Eq. (13).

this issue is still present even when accounting for the moment of inertia of the braces. A potential solution could be the inclusion of a tuning factor in the mass matrix to correct for the difference in the mass distribution. Since the mass matrix term related to torsion is uncoupled from the others, the proposed correction should improve the prediction of the torsional modal amplitude without affecting the other modes. This should be the subject of further expansion of the proposed model.

Finally, as discussed in Section 4, the use of the minimization strategy to improve the estimation of the elastic coefficients of the beam is only feasible whenever information on the natural frequencies of the space-frame structure is available. Whenever this information is not always available, an alternative strategy is required. Therefore, a multivariate nonlinear regression analysis was

performed to obtain a surface response model for the prediction of the calibration factors used to correct these elastic coefficients. This model was trained with data referring to the case of a straight structure only. A polynomial equation able to estimate the calibration factors for a large range of structures was found. This relies on five input parameters: the diameter of the legs, the diameter of the braces, the bay height, the bay width and, the number of bays. Within a specific range, representative of typical (offshore) wind support structure dimensions, it was possible to correctly predict any of the first five natural frequencies with a maximum 5% relative error within a confidence interval of at least 84%. Despite the results seeming promising, it should be noted that the intent of the presented preliminary data-driven model is to show the viability and potential of this approach. Better approaches, e.g., spline interpolation or Gaussian Processes regression, could be used to capture the highly nonlinear behaviour of the training dataset. A future research line in this regard is given by the potential offered by physics-informed machine learning techniques, which would allow for an improvement of the prediction capacity of the nonlinear regression model described in this paper.

5.2. Conclusions

In this work, a low-fidelity modelling approach for space-frame (offshore) wind support structures was proposed. The model is based on a geometrical and mass homogenization of a space-frame structure into an equivalent Timoshenko beam-like structure. The introduction of a partial isotropic behaviour in the LFM is necessary to account for the low-frequency torsional mode typical of space-frame structures. The shear and torsional rigidity were first guessed by means of Noor's expressions. The adopted elastic properties of the equivalent beam are then corrected by solving a minimization problem that leads to ad hoc correction/calibration factors able to improve the first guess of the elastic beam coefficients. An alternative strategy to bypass the latter optimization problem was also discussed, by adopting a trained multivariate regression model able to predict the needed calibration factor. Overall, in terms of computational cost with reference to the high-fidelity model, a significant speed-up of the LFM was observed by a factor of at least 60.

The calibrated LFM was tested for both straight and tapered space-frame structures. Three different rotor-nacelle assembly (RNA) configurations of increasing complexity were considered for the straight structure. For the tapered space-frame case, only the most detailed RNA was considered, namely RNA2. The LFM and the HFM were compared in terms of eigenfrequencies, shape of the corresponding eigenmodes, modal assurance criterion (MAC) and response to various dynamic loads. The quantitative comparison of the prediction errors mainly refers to the capacity of estimating the target eigenfrequencies and the dynamic response due to operational loads. For both straight and tapered structures, whenever the reference natural frequencies are known and an optimization procedure is applied, the LFM leads to minimal prediction errors for the target eigenfrequencies, i.e., below 1%. In terms of eigenmodes, the LFM was also very accurate in capturing both the shape and modal amplitude of the bending modes. However, while the shape of the torsional mode was correct, its modal amplitude differs from that of the HFM. With reference to the prediction of the dynamic displacements (maximum and mean values, and standard deviation), driven by operational loads, the LFM developed through the optimization procedure leads to minimal errors, the majority of which lie below 5%. For the specific case of a straight lattice tower, if the reference natural frequencies are not known, analytical expressions to estimate the equivalent elastic properties were used, leading to mean prediction errors for the first two bending modes and the torsional mode equal to, 5.2%, 13.3% and 18.8%, respectively. Whereas in the case of a tapered lattice tower, the mean prediction errors were approximately 6.0%, 14.7% and 8.7% for the first, third and fourth modes, respectively. It was shown that these errors can be significantly reduced by adopting a trained multivariate regression model, enabling the prediction of the calibration factors based on the geometrical details of the structure. In the case of a straight tower, the use of estimated calibration factors thanks to the developed regression model led to mean prediction errors below 5% for the entire investigated parameter space.

Declaration of competing interest

The authors declare that they have no known competing financial interests or personal relationships that could have appeared to influence the work reported in this paper.

Data availability

Data and codes can be found on 4TU.ResearchData and github respectively (see list of references).

Appendix. Polynomial coefficients

Table A.8 presents the coefficients found for targets γ_i. Here, the predictors, x_1, x_2, x_3, x_4 and x_5, are w_{bay}, h_{bay}, n_{bays}, D_{legs} and D_{braces} respectively.

Table A.8
Polynomial terms for the prediction of the γ coefficients.

PolyTerms	Prediction γ_1	Prediction γ_2	Prediction γ_3
Constant	1199/1047	2341/1645	491/744
x_1	−37/4815	−494/8917	−277/3398
x_2	132/10733	0	63/5387
x_3	−227/11122	521/11391	159/16516
x_4	−431/5464	−1811/7300	1768/1915
x_5	582/6049	536/803	−1315/1332
x_1x_2	−15/44327	−62/18069	24/59123
x_1x_3	−46/62187	73/13353	21/16643
x_1x_4	219/23053	−130/2279	−32/18411
x_1x_5	−578/16261	731/11617	110/7013
x_2x_3	−13/42433	−76/16547	29/15520
x_2x_4	−76/32753	77/2161	−208/16079
x_2x_5	235/24462	−145/2814	81/4988
x_3x_4	0	367/5409	−235/18578
x_3x_5	47/4338	−127/990	−161/13352
x_4x_5	−756/4075	369/1088	−236/9177
x_1^2	111/80254	225/61424	23/36976
x_2^2	−13/41556	26/12557	−11/24374
x_3^2	23/26104	−130/33831	0
x_4^2	85/2033	−568/5879	−183/4606
x_5^2	480/1987	−261/2003	707/7235

References

[1] Shields M, Beiter P, Nunemaker J, Cooperman A, Duffy P. Impacts of turbine and plant upsizing on the levelized cost of energy for offshore wind. Appl Energy 2021;298:117189.
[2] Siemens Gamesa Renewable Energy. SG 14-222 DD. 2020, URL https://www.siemensgamesa.com/en-int/products-and-services/offshore/wind-turbine-sg-14-222-dd. [Accessed 30 November 2022].
[3] Vestas. News release from vestas wind systems a/s. 2021, URL https://shorturl.at/bepDU. [Accessed 30 November 2022].
[4] Sunter M, Dose B. Validation and development of improved methods for the calculation of wave loads on XXL monopiles. In: Proc. of int. conf. on ocean, offshore and Arctic engineering, vol. 1618, no. 5. 2018.
[5] Ahmed SS, Hawlader B. Numerical analysis of large-diameter monopiles in dense sand supporting offshore wind turbines. Int J Geomech 2016;16(5):04016018.
[6] Damiani R, Dykes K, Scott G. A comparison study of offshore wind support structures with monopiles and jackets for U.S. waters. J Phys Conf Ser 2016;753(092003).
[7] Muskulus M. The full-height lattice tower concept. Energy Procedia 2012;24:371–7, Selected papers from Deep Sea Offshore Wind RI&D Conference, Trondheim, Norway, 19-20 January 2012.
[8] Natarajan A, Stolpe M, Njomo Wandji W. Structural optimization based design of jacket type sub-structures for 10 MW offshore wind turbines. Ocean Eng 2019;172:629–40.
[9] Vergassola M, Cabboi A, van der Male P. Comparative analysis of offshore support structures for two-bladed large wind turbines (10+MW) in deep waters. J Phys Conf Ser 2020;1618(5).
[10] Mühle F, Adaramola SM, Sretran L. The effect of the number of blades on wind turbine wake - a comparison between 2-and 3-bladed rotors. J Phys Conf Ser 2016;753(3):032017.
[11] Anstock F, Schütt M, Schorbach V. A new approach for comparability of two- and three-bladed 20 MW offshore wind turbines. J Phys Conf Ser 2019;1356(1):012008.
[12] Larsen TJ, Kim T. Experimental and numerical study of a new dynamic phenomenon for two-bladed wind turbines. Proc Int Offshore Polar Eng Conf 2015;2015-Janua:547–53.
[13] Prendergast L, Gavin K, Doherty P. An investigation into the effect of scour on the natural frequency of an offshore wind turbine. Ocean Eng 2015;101:1–11.
[14] Tatsis K, Ou Y, Dertimanis VK, Spiridonakos MD, Chatzi EN. Vibration-based monitoring of a small-scale wind turbine blade under varying climate and operational conditions. Part II: A numerical benchmark. Struct Control Health Monit 2021;28(6).
[15] Cong S, James Hu S-L, Li H-J. Using incomplete complex modes for model updating of monopiled offshore wind turbines. Renew Energy 2022;181:522–34.
[16] Peherstorfer B, Willcox K, Gunzburger M. Survey of multifidelity methods in uncertainty propagation, inference, and optimization. Siam Rev 2018;60(3):550–91.
[17] Jasa J, Bortolotti P, Zalkind D, Barter G. Effectively using multifidelity optimization for wind turbine design. Wind Energy Sci 2022;7(3):991–1006.
[18] Padron AS, Alonso JJ, Palacios F, Barone MF, Eldred MS. Multi-fidelity uncertainty quantification: application to a vertical axis wind turbine under an extreme gust. In: 15th AIAA/ISSMO multidisciplinary analysis and optimization conference. 2014, p. 3013.
[19] Murty MKS. Dynamic response of lattice towers and guyed masts. American Society of Civil Engineers; 2002.
[20] Sackmann V. Prediction of natural frequencies and mode shapes of self-supporting lattice telecommunication towers. Project report G, Department of Civil Engineering and Applied Mechanics, McGill University; 1996.
[21] Noor AK, Anderson MS, Greene WH. Continuum models for beam- and platelike lattice structures. AIAA J 1978;16(12):1219–28.
[22] Noor AK, Andersen CM. Analysis of beam-like lattice trusses. Comput Methods Appl Mech Engrg 1979;20(1):53–70.
[23] Salehian A, Inman DJ. Dynamic analysis of a lattice structure by homogenization: Experimental validation. J Sound Vib 2008;316(1):180–97.
[24] Sun CT, Juang JN. Modeling global structural damping in trusses using simple continuum models. AIAA J 1986;24(1):144–50.
[25] McCallen D, Romstad K. A continuum model for the nonlinear analysis of beam-like lattice structures. Comput Struct 1988;29(2):177–97.
[26] Moreau G, Caillerie D. Continuum modeling of lattice structures in large displacement applications to buckling analysis. Comput I Struct 1998;68(1):181–9.
[27] Guzmán A, Rosales M, Filipich C. Continuous one-dimensional model of a spatial lattice. Deformation, vibration and buckling problems. Eng Struct 2019;182:290–300.
[28] Lee U. Equivalent continuum representation of lattice beams: spectral element approach. Eng Struct 1998;20(7):587–92.

[29] Stephen N, Wang P. On transfer matrix eigenanalysis of pin-jointed frameworks. Comput Struct 2000;78(4):603–15.
[30] Jalbi S, Bhattacharya S. Closed form solution for the first natural frequency of offshore wind turbine jackets supported on multiple foundations incorporating soil-structure interaction. Soil Dyn Earthq Eng 2018;113:593–613.
[31] Besselink B, Tabak U, Lutowska A, van de Wouw N, Nijmeijer H, Rixen D, et al. A comparison of model reduction techniques from structural dynamics, numerical mathematics and systems and control. J Sound Vib 2013;332(19):4403–22.
[32] Timoshenko S, Goodier JN. Theory of elasticity. 3rd ed.. New York: McGraw-Hill; 1970.
[33] Box G, Draper R. Empirical model-building and response surfaces. John Wiley & Sons; 1987.
[34] Ewins DJ. Modal testing: theory, practice, and application. 2nd ed.. Baldock, Hertfordshire, England; 2000.
[35] Versteijlen W, Metrikine A, van Dalen K. A method for identification of an effective Winkler foundation for large-diameter offshore wind turbine support structures based on in-situ measured small-strain soil response and 3D modelling. Eng Struct 2016;124:221–36.
[36] Balmès E. High modal density, curve veering, localization: A different perspective on the structural response. J Sound Vib 1993;161(2):358–63.
[37] Triantafyllou M, Triantafyllou G. Frequency coalescence and mode localization phenomena: A geometric theory. J Sound Vib 1991;150(3):485–500.
[38] Rasmussen CE, Williams CKI. Gaussian processes for machine learning. MIT Press; 2005.
[39] Allen M. Understanding regression analysis. New York: Plentum Press; 1997.
[40] Kamariotis A, Chatzi E, Straub D. Value of information from vibration-based structural health monitoring extracted via Bayesian model updating. Mech Syst Signal Process 2022;166:108465.
[41] Vergassola M. A low-fidelity model for the preliminary design phase of full-lattice wind support structures: dataset used for the data-driven model. 2022, http://dx.doi.org/10.4121/21644789.
[42] Vergassola M. Lofi - low-fidelity model of a full-lattice support structure for (offshore) wind applications. 2022, https://github.com/mvergassola/LoFi.git.